Revision 1

Genetic implications, composition, and structure of trioctahedral micas in xenoliths related to Plinian eruptions from the Somma-Vesuvius volcano (Italy)

Giuseppina Balassone[1,2,3*], Emanuela Schingaro[4], Maria Lacalamita[4], Ernesto Mesto[4], Angela Mormone[2], Monica Piochi[2], Vincenza Guarino[1], Annamaria Pellino[1], Loredana D'Orazio[3]

[1] Dipartimento di Scienze della Terra, dell'Ambiente e delle Risorse, Università degli Studi di Napoli Federico II, via Cintia 26, 80126 Napoli, Italy

[2] Istituto Nazionale di Geofisica e Vulcanologia, Osservatorio Vesuviano, via Diocleziano 328, I-80124 Napoli, Italy

[3] Istituto per i Polimeri Compositi e Biomateriali IPCB, CNR, via Campi Flegrei, 34, 80078 Pozzuoli, Napoli, Italy

[4] Dipartimento di Scienze della Terra e Geoambientali, Università degli Studi di Bari, via Orabona 4, I-70125 Bari, Italy

* Corresponding author: balasson@unina.it

RUNNING TITLE: Genetic implications and crystal-chemistry of Vesuvius micas

ABSTRACT

The present work is part of a systematic mineralogical and petrographic characterization of mica-bearing xenoliths from Somma-Vesuvius volcano (Roman Magmatic Province, southern Italy).

Skarns, composite skarns-marbles and cumulates from Pompeii Plinian eruption (AD 79), and skarns and syenite from Avellino eruption (3945 ± 10 cal yr BP) were investigated to define the crystal chemistry of the Somma-Vesuvius trioctahedral micas and to draw inferences on petrogenetic processes they were subjected. Xenoliths were characterized by means of polarized optical microscopy, scanning electron microscopy (SEM-EDS), X-ray powder diffraction (XRPD) and bulk-rock geochemical analyses. Mica crystals were studied through electron microprobe analysis (EMPA) and single-crystal X-ray diffraction (SCXRD).

Micas from skarns are variably associated with Mg±Ca silicates (clinopyroxene, vesuvianite, humite, clinohumite, chondrodite, forsterite, garnet), other sporadic silicates (anorthite, sodalite, titanite, britholite), apatite, calcite, various types of oxides, as well as rare sulfides and halides. In composite skarn-marble rocks, the mineral assemblages show some differences compared to skarns, as lack of clinopyroxene and the presence of dolomite. Cumulate samples consist of mica and clinopyroxene, whereas syenite is mainly composed of mica, K-feldspar, feldspathoids and clinopyroxene. Together with mica, apatite occurs in all the lithotypes.

Trace element arrays are scattered for skarn and composite skarn-marble samples. The REE patterns have a general enrichment in light (La, Ce, Pr, Nd) and medium (Sm, Eu, Gd, Tb, Dy) rare earth elements, in some case with slight positive Gd anomaly. Cumulate samples generally have low amounts of Ba, Sr, Zr and Th, while syenite exhibits low concentrations of trace elements, except for Rb, Cs and Tl.

Mica crystals occurring in the studied xenoliths are phlogopite with different Al and Mg content at the octahedral site, a negligible tetraferriphlogopite component and variable dehydrogenation degree. All samples belong to the 1*M* polytype (*C*2/*m* and *C*2 space group) and have a wide range of unit cell parameters, especially of the *c* axis [$5.3055(1) \leq a \leq 5.3218(1)$ Å, $9.1893(1) \leq b \leq 9.2188(4)$ Å, $10.1803(2) \leq c \leq 10.2951(2)$ Å]. The shortest *c* cell parameter pertains to de-hydrogenated phlogopite from Avellino skarn whereas OH-rich phlogopite from Pompeii composite skarns-marbles has a *c* cell parameter which approximates that of the endmember phlogopite.

Overall, it is observed that the crystal chemistry of the micas of the present study extend the known range of the other Vesuvian micas from literature. The Ti-depletion and the wide degree of dehydrogenation of phlogopites from skarns and composite skarns-marbles suggest that the studied samples originated under variable pressure conditions. In addition, the presence of humite in the mineral assemblage seems to indicate the occurrence of devolatilization reactions. The scarce mica occurrence in cumulate and mainly in syenite, instead, may depend on pressure conditions in the magma storage system exceeding the mica stability.

Keywords: phlogopite, crystal chemistry, ejecta, Vesuvius.

INTRODUCTION

Micas are common minerals in magmatic rocks from a wide range of physico-chemical conditions and their importance as petrogenetic indicators is widely accepted (e.g., Lepore et al., 2017, and references therein; Guarino and Brigatti, 2018; Lacalamita et al., 2020). In the peridotite mantle, micas are stabilized at the expense of olivine and pyroxene in presence of hydrous silica-rich metasomatizing agents (e.g., Sekine and Wyllie, 1982) and provide important information on the early fractionation history of ultrapotassic rocks (Fritschle et al., 2013). According to various authors (e.g., Fritschle et al., 2013; Lepore et al., 2017 and references therein), micas of the phlogopite-annite series are particularly useful to define igneous processes leading to the wide compositional spectrum of ultrapotassic rocks. Therein, several crystal chemical studies exist on micas from different ultrapotassic rocks such as kamafugites (e.g., Lacalamita et al., 2012; Schingaro et al., 2011; Scordari et al., 2012), lamproite-like rocks (e.g., Babushkina et al., 2000; Brigatti et al. 1991; Brigatti and Poppi, 1993; Cruciani and Zanazzi, 1994; Schingaro et al., 2014),

leucitites (e.g., Brigatti et al., 2005; Laurora et al., 2009), Mica-Rich Enclaves (MRE; e.g., Laurora et al., 2007), as well as on micas from alkaline-carbonatite complexes (Guarino and Brigatti, 2018).

The role of phlogopite in petrogenetic processes is strictly associated to the multiple concurrent ionic substitutions occurring in the crystal structure: $M^{3+,4+}$-Tschermak (e.g., Abrecht and Hewitt, 1988; Dymek, 1983; Matarrese et al., 2008; Waters and Charnley, 2002), $M^{3+,4+}$ ↔ vacancy (Waters and Charnley, 2002) and $M^{3+,4+}$-oxy (e.g., Ventruti et al., 2008 and references therein). However, the definition of the substitutions in the crystal structure of phlogopite requires the combination of structural analyses, along with a complete determination of the chemical composition including the analysis of the H_2O content and of the iron speciation, often limiting the application of phlogopite as petrogenetic indicator. In the literature only two complete crystal chemical studies on mica from lamproite rocks (Lepore et al., 2017) and xenolithic ejecta (Balassone et al., 2013) exist. The characterization of phlogopite from three main lamproite rocks - Western Alps, Tuscany, and Northern Latium (northern-central Italy) as well as Corsica (France) - was undertaken by Lepore et al. (2017), with the aim of shedding light on the possible different origin of micas in relation with the different lamproite-like magmas (e.g., Conticelli et al., 2009).

Balassone et al. (2013) proposed the first crystal-chemical and petro-volcanological investigations of trioctahedral micas from the Somma-Vesuvius volcano, one of the most famous worldwide volcanoes located in Italian volcanic belt (at the southern end of the Roman Magmatic Province; Conticelli et al., 2011, and references therein) and associated with the high potassic magmatism developed in the Central Mediterranean area. These authors, by considering different xenolithic ejecta (metamorphic/metasomatic skarns, pyrometamorphic/hydrothermally altered, mafic cumulates) associated to historical lavas of the most recent volcanic activity, AD 1631 – 1944, found that the variability of the crystal chemical features of micas was consistent with the remarkable variation of their host rocks and magma storage conditions.

The present work aims at continuing the previous study on the Somma-Vesuvius micas by focusing on xenoliths from the older and larger eruptions, i.e., the so-called Pompeii and Avellino

Plinian eruptions (AD 79 and 3945 ka, respectively). This research wants to improve the knowledge of the crystal chemistry of the Somma-Vesuvius trioctahedral micas and to draw inferences on genetic processes they were subjected to, also offering insights to understanding other similar volcanic systems.

BACKGROUND INFORMATION

Geological and volcanological outline

The Italian Peninsula is unique in the world for the high number, more than fifty, of recent to active volcanoes characterized by extremely different petrochemical features and eruption styles. In this area, the magmatism is alkaline-potassic and developed from Oligocene to present, with the last eruption of leucite-bearing magmas occurring in AD 1944 at Vesuvius (Avanzinelli et al., 2017, and references therein). Vesuvius, or also Somma-Vesuvius (Fig. 1), is a stratovolcano built-up on the Mesozoic carbonate sedimentary sequence of the Campanian Plain (Brocchini et al., 2001). Somma is the old edifice dissected by volcanic collapses consequent the emptying of magma chamber during high-magnitude Plinian eruptions (e.g., Cioni et al., 1999); Vesuvius *s.s.* is the most recent cone, discontinuously growth inside the caldera until the AD 1944. The volcano produced largely variable magnitude eruptions from high-VEI Plinian and sub-Plinian to low-VEI lava effusion and strombolian to vulcanian events; the last ones characterized the periods of semi-persistent open-conduit - known as “inter-plinian” - volcanism (Santacroce, 1987). The classical and best-studied “inter-plinian” volcanism started after the AD 1631 sub-plinian event and lasted until the most recent eruption in AD 1944 (Arrighi et al., 2001).

Based on the rock-geochemistry of the erupted products (Ayuso et al., 1998; Piochi et al., 2006a,b; Di Renzo et al., 2007; Santacroce et al., 2008), different volcanic periods were established: the oldest one (>8-9 ka) produced slightly undersaturated rocks from K-basalt to K-trachyte, the

period between 8-9 ka and the AD 79 involved K-phonolite-tephrite to K-phonolite magma compositions, and the period younger than AD 79 characterized for highly undersaturated magmas, from leucititic tephrite to leucititic phonolite. Overall, a wide range of Sr and Nd isotope compositions have been documented, from 0.7066 to 0.7081 and 0.5126 to 0.5124 respectively (Ayuso et al., 1998; Piochi et al., 2006a, b; Di Renzo et al., 2007). The compositions mostly reflect evolutionary processes that occurred during upward migration to shallow crustal levels in primary magmas bearing contributions from different mantle reservoirs and slab-derived components. Some authors ascribed the variations of Sr-Nd-Pb-O isotopic compositions in central Italian magmas (including Somma-Vesuvius) to crustal assimilation of carbonates during storage in the upper few kilometres of the crust (e.g., Piochi et al., 2006a; Di Renzo et al., 2007; Iacono-Marziano et al., 2008, 2009; Scaillet et al., 2008; Dallai et al., 2011; Pichavant et al., 2014); other researchers favor isotopic variability of associated mantle sources (e.g., Peccerillo, 2005; Moretti et al., 2013). Refilling and mingling processes between different magmas within each volcanic period or eruption event are evident from isotope variations (Cioni et al., 1999; Piochi et al., 2004; Pappalardo et al., 2004 and references therein). Recent studies involved the petrological and geochemical evolution of the chemically zoned juvenile samples come from Plinian and sub-Plinian eruptions (Melluso et al., 2022). These authors point to the existence of a similar mineralogical paragenesis in the different eruptions, but these minerals have different composition, suggesting the existence of independent, zoned magma batches throughout the activity of the stratovolcano, which possibly started to crystallize at similar depths.

However, the processes also involved carbonate contamination and entrapment of crystal mush generated during previous magma storage in the crust (Jolis et al., 2013; Piochi et al., 2006a).

The “Avellino” (3945 ± 10 cal yr BP; Di Vito et al., 2019, and references therein) and “Pompeii” (AD 79) are probably the most famous and widespread plinian eruptions of Somma-Vesuvius, with the white and grey pumice deposits associated with sustained pyroclastic column and variable collapsing styles (Gurioli et al., 2005; Sulpizio et al., 2010; Balcone-Boissard et al.,

2012 and references therein; Massaro et al., 2018; Doronzo et al., 2022). White pumices were emitted prior to grey pumices, both phonolitic, but with the white type having a higher differentiation degree (Cioni et al., 2008; Balcone-Boissard et al., 2012). According to the above authors, the volume of fallout tephra is 1.5 km^3 for Avellino and 3.3 km^3 for Pompei. The Avellino products contain sanidine and minor nepheline, clinopyroxene, biotite, amphibole, and oxides; minerals of marialite-meionite ("scapolite") have also found. The Pompeii tephra contains sanidine, pyroxene, phlogopite, K-ferripargasitic amphibole, melanitic garnet and leucite in the groundmass. Similarly to "Pomici di Base" (18.3 ka bp) and "Mercato" (8 ka bp), they determined caldera collapses and dissection of the limestone basement (Cioni et al., 1999) in which their feeding magma chambers were stored and evolved (Cioni et al., 1995; Cioni, 2000; Piochi et al., 2006a, b; Fulignati et al., 2005; Signorelli et al., 1999; Balcone-Boissard et al., 2012; Vona et al., 2020).

The Somma-Vesuvius ejecta

A large variety of xenolith types is present in the Somma-Vesuvius eruptive products, including weakly-to-highly metamorphosed carbonate, skarns, plutonic rocks (cumulates, alkali syenites), lavas/pyroclasts (Jolis et al., 2015 and references therein), as well as hornfelses (Del Moro et al., 2004) and sedimentary rocks (Barberi et al., 1981; Joron et al., 1987). Composite xenoliths are also frequently found at Somma-Vesuvius, having sharp transitions from skarns to marbles, hornfelses and igneous rocks; they document the close spatial association of these rock types at depth and provide unequivocal evidence for magma–carbonate interaction during magma differentiation (e.g., Gilg et al., 2001; Piochi et al., 2006a, b; Jolis et al., 2015).

The marbles derive from thermally affected limestone or dolostone of the Mesozoic basement that has undergone recrystallization and, in part, devolatilization, but overall reflecting relatively modest interaction with metasomatic fluids or silicate melts (Gilg et al., 2001; Jolis et al., 2015). Carbonate clasts occur in most depositional sequences of the Somma-Vesuvius, in agreement with

entrapment pressure of inclusions of 3.5-5 km and deeper than 7 km (e.g., Marianelli et al., 1999; Cioni, 2000; Fulignati et al., 2005) and Sr-isotope variation through magma storage depths (Piochi et al., 2006a). Based on several authors (e.g., Dallai et al., 2011; Jolis et al., 2013; Piochi et al., 2006a), Mesozoic carbonate rocks are the contaminant of magma in the roots of the volcanic structure, mostly at shallow depth. Volcanic rock geochemistry registered carbonate assimilation and is useful tool to study the consequent influence on the magma evolution, its volatile content and degassing modes, the eruption dynamics. However, limestone xenoliths allow detecting the possible physico-chemical changes produced by the magma and carbonate host interaction with implications on rock mechanics, hydrothermal circulation and mineral/metal ore developing. Some authors focused on mineralization and isotope deviance induced by thermo-metamorphism in carbonate xenoliths (e.g., Jolis et al., 2015 and references therein). From petrographic and mineralogical point of view, marble xenoliths mainly consist of calcite with a typical saccharoidal texture. Dolomite is also detected as relic crystals in metadolostone ejecta, characterized by calcite and periclase assemblage; brucite and hydromagnesite commonly occur as secondary retrograde rims around periclase (Gilg et al., 2001). Accessory minerals include diopside, phlogopite, forsterite, chondrodite, humite, clinohumite, norbergite, spinel, graphite, illite, and albite (Barberi and Leoni, 1980).

Hornfelses, rarely occurring at Somma-Vesuvius, consist of a fine-grained homogeneous granoblastic calc-silicate assemblage of diopside, quartz, feldspars, and wollastonite (Barberi and Leoni, 1980). Marbles and hornfelses are interpreted as thermally metamorphosed carbonate (limestone or dolostone) or marly rocks that have suffered recrystallization and in part devolatilization with modest metasomatic interaction with aqueous fluids or silicate melts (Gilg et al., 2001; Jolis et al., 2015).

Skarns have calc-silicate compositions typically developing in contact-metamorphic aureoles in response to interaction between limestone or dolostone with a silicate magma. The formation of these rocks is known to progressively modify the composition of both the magma and the carbonate

wall-rock. Skarn ejecta are common at Vesuvius and display a wide range of mineral compositions and textures also with zoning and metasomatic fronts (also few millimetres in thickness). Typical skarn Ca- and/or Mg-silicate crystal phases are clinopyroxene, phlogopite, wollastonite, olivine, clinohumite, vesuvianite, garnet, gehlenite, and anorthite; other skarn minerals can be calcite, dolomite, meionite, leucite, fluorapatite, titanite, cuspidine, perovskite, baddeleyite, geikelinte, zirconolite, calzirtite, etc. (Gilg et al., 2001; Pascal et al., 2011; Jolis et al., 2015 and references therein). Different varieties of spinels have been also described, i.e., spinel, magnetite, magnesioferrite and qandilite, the last two phases found in metasomatic forsterite-spinel-calcite skarns (Pascal et al., 2011). Many studies characterized pressure and temperature of skarn formation, the fluid nature and the isotope evolution related to the limestone/dolostone-skarn transition, as reported by Jolis et al. (2015 and references therein). Skarn xenoliths in the Vesuvius eruptive deposits can be linked to relatively shallow magma reservoirs (≤4–10 km; Auger et al., 2001; Civetta et al., 2004; Scaillet et al., 2008 and references therein) just developed within the thick limestone and dolostone carbonate sequence which extend from approximately ≥2 km to at least 8 km depth under the volcano (Zollo et al., 1996; Bruno et al., 1998; Auger et al., 2001; Brocchini et al., 2001).

The igneous ejecta are volcanic to plutonic (or hypabyssal) rocks; the last one consists of pyroxenites and alkali syenites. Pyroxenites are characterized by high proportions of clinopyroxene with minor phlogopite and are likely of cumulate origin. The alkali syenites are fine to medium grained and are dominated by subhedral to anhedral sanidine, garnet, and subordinate amphibole, sodalite group minerals (Balassone et al., 2012, 2016), nepheline, and leucite etc. They have been interpreted as part of a crystallizing magmatic mush.

As already stated, the mica-bearing samples considered in this study come from Avellino and Pompeii deposits (Table 1); these eruptions have brought a large amount of ejecta, especially of skarn type (Gilg et al., 2001; Jolis et al., 2015), to the surface (Joron et al., 1987). The mica varieties commonly observed at Somma-Vesuvius are phlogopite and “biotite” (Russo and Punzo,

2004). As reported by Gilg et al. (2001) for micas from skarn and composite ejecta, Mg-rich and Ti-poor phlogopite, typically occur in zoned skarn ejecta associated to diopsidic/hedenbergitic to (less common) "fassaitic" clinopyroxene, F-bearing vesuvianite, wollastonite, gehlenite, meionite, forsterite, clinohumite, anorthite, and Mg-poor calcite, with many accessory minerals (i.e., apatite, spinel, magnetite, perovskite, baddeleyite, and various undefined REE-, U-, Th-, Zr-, and Ti-rich minerals).

SAMPLES AND EXPERIMENTAL METHODS

The analyzed micas occur in xenoliths collected from outcrops close to Somma Vesuviana, Ercolano and Terzigno towns (Fig. 1), i.e., in skarns, cumulates, syenites, and composite (marble-skarn) lithotypes (see Table 1 and Fig. 2a). After preliminary mesoscopic observations, a combination of polarized optical microscopy, X-ray powder diffraction (XRPD) and scanning electron microscopy equipped with an energy-dispersive spectrometer (SEM-EDS) was used to characterize the mica-bearing xenoliths from the textural, mineralogical, and petrographic point of view.

Bulk rock geochemistry was carried out at two laboratories, i.e. Activation Laboratories LTD (Ancaster, Canada) and Bureau Laboratories Ltd. (Vancouver, Canada). At Activation Laboratories (sample set PS40, PS41, PS44, PS50, PS54, PS55, PS57, PS58, PS60, PS80, PS81, PS82, PS84, PSK-R), major elements were analyzed via ICP-OES (inductively coupled plasma-optical emission spectrometry) using a Thermo Jarrell-Ash ENVIRO II ICP. Trace elements were determined by ICP-MS with a Perkin Elmer SCIEX ELAN 6000. Uncertainty is less than 3% for major oxides, less than 15% for Co, Y, Zr, and Tb, and less than 5% for all other trace elements (see www.actlabs.com). At Bureau Laboratories (sample set PS62, PS65, PS68, PS70, PS73, PS77), major elements were analyzed by X-ray fluorescence (XRF) and inductively coupled plasma

emission spectrometry (ICP-ES), using $LiBO_2/Li_2B_4O_7$ fusion. Minor and trace elements were determined by inductively coupled plasma-mass spectrometry (ICP-MS), using a four-acid (HNO_3-$HClO_4$-HF-HCl) digestion. Loss on ignition (LOI) was calculated by weight loss after ignition at 1000°C. The uncertainty is less than 3% for major/minor oxides, less than 5-10% for trace elements (see http://acmelab.com). In both cases, loss on ignition (LOI) was calculated by weight loss after ignition at 1000°C.

XRPD was conducted on powdered rocks using a Seifert-GE diffractometer ID 3003 (DiSTAR, University of Naples, Italy). Intensity profiles were collected in the 2θ range of 3-80° using Ni-filtered CuKα radiation at 40 kV and 30 mA, with a step size 0.02°, at a scanning time of 10 s/step. The diffraction patterns were processed using the RayfleX software package. A minor set of measurements were performed by using a X'Pert Powder diffractometer by PANalytical (Istituto Nazionale di Geofisica e Vulcanologia, Osservatorio Vesuviano, Napoli, Italy), equipped with a high speed PIXcel detector, Ni-filtered, CuKα radiation (40 kV and 40 mA in the 3-70 °2θ range, 0.02° steps at 8 s/step) and a PANalytical B.V. software HIGHScore Plus version 4.9 for the elaboration of the diffraction profiles (Mormone et al., 2014).

Electron dispersive spectroscopy (EDS) microanalyses and backscattered electron images (BSE) of the whole mineral assemblages in thin sections were obtained with an INCA X-stream pulse processor and the 4.08 version Inca software (Oxford Instruments detector), interfaced with the JEOL JSM 5310 (DiSTAR, Naples, Italy). Observations were made in backscattered electron mode (BSE), at accelerating voltage 15 kV, 50–100 μA filament current and variable spot size and a working distance of 20 mm. The following reference standards were used: albite (Si, Al, Na), orthoclase (K), wollastonite (Ca), diopside (Mg), almandine (Fe), rutile (Ti), barite (Ba), strontianite (Sr), metallic chromium (Cr), rhodonite (Mn), pyrite (S), sphalerite (Zn), galena (Pb), fluorite (F), apatite (P), sylvite (Cl), Smithsonian phosphates (La, Ce, Nd, Sm, Y), gallium arsenide (As), and metallic vanadium (V). Analytical errors are 1% relative for major elements and 3% relative for minor elements.

In order to determine the chemical composition by electron microprobe analysis (EPMA) of mica crystals, they were selected under the binocular microscope from the grains of crushed rocks, and then prepared as polished opaque mounts (by means of Bueheler EpoKwich™ epoxy resin, as well as Bueheler polishing cloths and diamond suspensions). Chemical analyses were carried out using a Cameca SX50 WDS instrument (CNR-IGAG, Rome) under the following experimental conditions: 15 nA sample current, 10 kV accelerating voltage, 10 μm beam diameter; no Na loss was detected during the analyses. From each sample, we selected three to five mica grains, and performed five to eight microanalyses, reporting the averages in Table 3. The standards were: wollastonite (Si, Ca), titanite (Ti), corundum (Al), magnetite (Fe), periclase (Mg), jadeite (Na), and orthoclase (K). Data were corrected using the PAP program (Pouchou and Pichoir, 1991). Relative uncertainty on the analytical measurements was 1% for major elements, 4% for minor elements, and 10% for F.

Scanning electron microscopy (SEM) examination of morphological features of selected mica crystals were carried out by means of both the JEOL JSM 5310 instrument, and a small subset of samples was also observed bFEI Quanta 200 SEM (IPCB-CNR Pozzuoli, Italy).

Single crystal X-ray diffraction (SCXRD) data were collected on mica crystals from selected rocks (PS68, PS77, PS50, PS62, PS73) both from Avellino and Pompeii eruptions by means of a Bruker AXS X8 APEXII automated diffractometer (Dipartimento di Scienze della Terra e Geoambientali, University of Bari, Italy), equipped with a CCD detector and graphite-monochromatized Mo Kα radiation (λ = 0.71073 Å) operating at 50 kV, 30 mA and 40 mm crystal-to-detector distance. The whole Ewald sphere (±h,±k,±l) was recorded up to θ~45° with a scan width 1.0°/frame and an exposure time 20 s/frame. The APEX program suite allowed to optimize the collection strategy (Bruker, 2010); the SAINT package (Bruker, 2007) was used for the integration of the intensities of reflections and the correction of the Lorentz and polarization effects; the SADABS software (Bruker, 2009) was employed for the empirical absorption correction;

XPREP (Sheldrick, 2008) was used for the subsequent analysis of the intensity data and the assignment of the space group.

In the case of PS50 sample, CELL_NOW program (Sheldrick, 2003a) identified two twinned individuals rotated of 180° around a twin axis parallel to [310]; the TWINABS software provided for a semi-empirical absorption correction (Sheldrick, 2003b).

Structure refinements were carried out in *C*2/*m* space group by means of the program CRYSTALS (Betteridge et al., 2003) considering the reflections with $I > 3\sigma(I)$. Overall scale factor, atomic positions, cation occupancies and anisotropic atomic displacement parameters were refined, starting from the coordinates of micas belonging to the phlogopite-fluorophlogopite series in Lacalamita et al. (2020). The occupancy of the tetrahedral site was constrained to 1; the Mg vs. Fe occupancies in the octahedral site were varied with full occupancy constraint for all samples except for PS50 where only Mg was refined both in *M*1 and *M*2; a restraint (1.00 ± 0.08) on the occupancy of the K atoms at the interlayer site was used to allow the occupancy of this site to assume values higher or lower than 1. The analysis of the difference-Fourier maps for all samples except for PS77 evidenced the presence of a residual electron density peak ~ 1 $e^-/Å^3$ which may be considered as the position of the hydrogen atom, at ~ 0.9 Å from the O4 oxygen. It was included in the refinement using the strategy of refinement described elsewhere (Lacalamita et al., 2020).

For PS77 sample, at the end of the refinement in *C*2/*m* space group, an *R*-value of 4% was obtained; analysis of the difference Fourier synthesis showed two peaks ~ 3.5 and 1.5 $e^-/Å^3$ at 0.57, 0, 0.22 and 0, 0.16, 0, respectively. These peaks are hints of ± *b*/3 shifts of the octahedral sheet, which leads to desymmetrization of the whole structure (Schingaro et al., 2001). Therefore, a reduction of symmetry from *C*2/*m* to *C*2 was attempted considering extra (disordered) atoms with respect to the ordered part of the structure. The latter was refined using proper constraints to impose the *C*2/*m* symmetry. The final refinement converged to *R* 2.9% and no significant residual electron density was observed. The same disorder affected the PS73 although at minor extent (residual peaks ≤ 1.3 $e^-/Å^3$). Since the electron density of the disorder atoms was ≤ 0.2 e^-, the disorder modelling

was not included in the final refinement of this sample. Crystallographic interchange format (CIF) files are also provided as supplementary materials.

RESULTS AND DISCUSSION

The xenoliths

Petrographic description

The Pompeii xenolithic samples (# 12 samples) are represented by three lithologies, i.e., skarns, composite skarns-marbles and cumulates, whereas the Avellino samples (# 8 samples) mostly consist of skarns and one syenite (Fig. 2b). SEM-BSE micrographs of selected samples in thin sections are shown in Fig. 3.

The skarn samples are characterized by a texture variable from granoblastic with equigranular crystals of phlogopite, clinopyroxene and calcite often randomly oriented (decussate texture), to poikiloblastic with small inclusions of various minerals mainly in larger megacrysts (Fig. 3a-h). These samples are mostly composed of Ca±Mg silicates, among which the most common are clinopyroxene, vesuvianite, humite, clinohumite, sodalite, forsteritic olivine, leucite, and garnet, detected in variable amounts (Table 1), locally accompanied by calcite and a wide variety of other µm-sized mineral phases, difficult to identify with just chemical analyses and optical observations. An association with phlogopite-clinopyroxene±spinel±calcite±apatite - recognized in many skarns of Somma-Vesuvius - was observed both in Pompeii and Avellino samples (Table 1 and Fig. 3a-h). Sodalite and anorthite occur in two Avellino skarns (Table 1 and Fig. 3b). Humite occurs in Avellino (PS55, PS77, PSK-R) and Pompeii (PS70, PS73) skarns, chondrodite in Avellino skarn PSK-R and clinohumite in the Avellino skarn PS41 (i.e., Fig. 3c,f). Titanite was found only in Avellino PS84 skarn, where rare mixed Ca-Ti and Zr-Ti oxides (as perovskite, pyrochlore

supergroup minerals, and zirconolite) also occur (Fig. 3g). Magnetite is present in Pompeii skarn PS58, PS68, and PS70 (Table 1). Baddeleyite (Fig. 3a,d,h) is quite common and observed in five skarn samples in tiny and disseminated crystals (Avellino: PS41, PS60, PS82, and PSK-R; Pompeii: PS84); thorianite also occurs in Pompeii skarn PS58 (Fig. 3c) in tiny individuals. Carbonates are represented by rare and small calcite crystals, observed in five samples both from Pompeii and Avellino eruptions (Table 1). Tiny pyrite inclusions were observed in Avellino skarns (PS60 and PSK-R) (Fig. 3d). Other trace minerals are cuspidine, as well as likely bismoclite (Table 1).

In composite Pompeii skarns-marbles (Table 1), the contacts between the two lithologies can be variously sharp, with the carbonate components relatively more (PS44, PS54, PS62, PS65) or less (PS40, PS50) prevailing over skarn-related assemblages (i.e., sample PS44 in Fig. 2). Calcite displays a granoblastic saccharoidal texture, occasionally very friable, and often with quite fine (< 500 μm) crystals (Fig. 3i,l,m); dolomite is recorded in samples PS44, PS50 and PS54 (Fig. 3k-m). A poikiloblastic texture is also observed (partly as in Fig. 3l). The silicate minerals include, together with mica, humite, clinohumite, chondrodite, forsteritic olivine, vesuvianite, titanite and meionite (Fig. 3i,j,l,m); Accessory spinel, magnetite, apatite, galena, pyrite, thorianite, baddeleyite, and stolzite are locally detected (Table 1 and Fig. 3i). An undetermined Si-Zn-Fe-Pb phase was observed in sample PS44 (Fig. 3j); this could correspond to a mixture of a silicate-rich phases alternating with sulfide-rich phases forming a colloform texture, but no reliable chemical analyses were carried out.

Syenite PS57, with holocrystalline texture, is composed of K-feldspar, feldspathoids (leucite, nepheline, and sodalite), phlogopite, clinopyroxene, with small amounts of apatite and britholite (Fig. 3n).

The two cumulate samples (Table 1) are basically formed by clinopyroxene and phlogopite (Fig. 3o, p); small inclusions and/or vuggy linings of apatite, sodalite, baddeleyite, bismoclite, and vesuvianite are locally found, together with trace amounts of late fluorite, mimetite, and sylvite (Table 1; Fig. 3,o,p).

Mineral chemistry

The main mineral compositions detected in the investigated mica-bearing lithics are illustrated in Tables S1-S4. Clinopyroxenes, recorded in skarns, syenite and cumulates of both Pompeii and Avellino ejecta (Table S1), have zoned diopside/hedenbergite compositions (i.e., Fig. 4b, h), or also subsilicic ferroan aluminian diopside ("fassaite") with significant Ca-Al-Tschermak exchange component (i.e., skarn PS60 and cumulate PS80; table S1). As reported by Gilg et al. (2001), the Vesuvian "fassaitic" skarn pyroxenes generally have higher Ti and lower Mn contents than Al-poor skarn diopsides.

Olivine was detected in skarns PS58, PS73, and PSK-R and in composite rock PS62 (Table 1); it has a forsteritic composition (Fo_{88-99}) comparable to forsterites from metasomatic cumulates and skarns, but Mg-richer than magmatic olivines (Fo_{67-87}) (Gilg et al., 2001, and references therein; Fulignati et al., 2005). Among various silicates detected in the analyzed xenoliths, Table S1 also has representative chemical analyses of anorthite, feldspathoids (sodalite, leucite, and nepheline), garnets (grandite), and humite. Anorthite, nepheline, spinel, and garnets have been already reported in skarns from AD 79 (Fulignati et al., 2005). However, apart from sodalite and humite, in our sample set, these silicates mostly occur in the Avellino ejecta (Table 1).

F-rich apatite, with low Cl amounts, was furthermore detected in ejecta from both eruptions (samples PS58, PS60, PS80, and PS84), whereas mimetite was found only in sample PS81 as last phase to crystallize (Table S2). In particular, the humite and clinohumite in carbonate-rich rocks is known in the literature (e.g., Rice, 1980; Young and Morrison, 1992), although in our samples not often associated with olivine and pyroxene.

Accessory baddeleyite, zirconolite, and pyrochlore supergroup minerals, testifying variable leaching/mobilization processes of HFSE elements (such as Ti, Zr, Nb) during metasomatism which concentrated these elements in the skarn as oxides (Pascal et al., 2009), are presented in Table S3,

together with magnetite, spinel, thorianite, and perovskite; sulfides are also sporadically found and represented by galena and pyrite (Tables 1 and S3).

Calcite can be found both in skarns and skarns-marbles (Tables 1 and S4); calcite exhibits the following oxide content: 0.09-3.43 wt% of MgO, 0-1.20 wt% FeO, 0-5.58 wt% MnO, and up to 1.13 wt% SrO and 1.21 wt% BaO. Dolomite, occurring only in three composite samples, has up to 1.40 wt% FeO, 0.04 wt% MnO and 0.18 wt% BaO.

The mineralogical assemblage of the Pompeii and Avellino skarn and composite xenoliths investigated in this study shows some differences from that reported in Balassone et al. (2013). Indeed, the xenoliths investigated here do not contain britholite and glass, instead detected in the Ca-Mg-silicate xenoliths from the AD 1631 and AD 1944 eruptions from Balassone et al. (2013); also cuspidine was found only in trace amounts in the studied samples.

Xenoliths geochemistry

The chemical composition of the studied xenoliths has a wide compositional range in terms of major elements contents, as SiO_2, CaO, and MgO (Fig. 4; Table 2), closely related to their complex mineralogical assemblages. Skarns and skarn-marble xenoliths from the Pompeii eruption are characterized by a broad compositional spectrum, with SiO_2, CaO, and MgO in the ranges 6.4-48.7 wt%, 4.2-38.1 wt% and 3.7-30.9 wt%, respectively. The highest CaO concentration is detected in rock samples with a composite nature, mainly reflecting the prevailing presence of calcite (and minor dolomite) in the marble components. The Avellino skarns have a SiO_2 narrower range of variation (30.1-44.6 wt.%) compared to the Pompeii xenoliths (Fig. 4a), also due to the absence of composite rocks in that analysed sample set, and CaO and MgO ranges of 3.7-23.4 wt.% and 8.9-31.2, respectively (Fig. 4b). The more frequent occurrence of pyroxene can justify the coupled higher SiO_2 and lower CaO content in the Avellino with respect to the Pompeii skarns (Table 1). In CaO vs. SiO_2 and MgO vs. CaO diagrams (Fig. 4a, b) Pompeii and Avellino skarns fall approximately close to the compositional field of AD 1631 skarns of Balassone et al. (2013, see

Fig. 4); some samples also plot in or very close to the AD 79 and AD 472 skarn field of Jolis et al. (2015), while the Pompeii composite ejecta PS44, PS54, and PS62 are close to the marble compositions of these authors.

The Avellino syenite sample (PS57) has the highest SiO_2 values (49.5 wt%) of the analyzed sample batch, and CaO and MgO values of 6.5 wt% and 4.6 wt%, respectively (Fig. 4a, b); it falls in the Somma-Vesuvius syenites-foidolites-essexites field from literature (see Fig. 4 in Balassone et al., 2013, and references therein), as well as in the igneous rocks compositional field of Jolis et al. (2015).

As regards the two Pompeii cumulate samples (PS80 and PS81), they have SiO_2, CaO, and MgO in the ranges 41.5-44.6 wt%, 4.1-12.3 wt% and 14.2-16.6 wt%, respectively, which are close to data from literature (Fig. 4a, b), also considering the igneous rocks compositional field of Jolis et al. (2015).

In the main variation diagrams of selected major elements against SiO_2 (Fig. S1 a-f); a semi-linear trend for K_2O, Na_2O, Al_2O_3, Fe_2O_3, and TiO_2 can be defined for the skarn and skarn-marble samples, with significantly higher values of K_2O for Pompeii sample PS73 and of Fe_2O_3 for Pompeii samples PS58 and PS73. The MgO concentrations in the skarn suite are more scattered, as similarly observed by Jolis et al. (2015). A negative trend can be also observed in Fig. S1 g-j, where K_2O, Na_2O, Al_2O_3, Fe_2O_3 are plotted against CaO concentrations. In general, some samples with composite nature (i.e., PS44, PS62, and PS62) are featured by low amounts in major elements oxides as K_2O, Na_2O, Al_2O_3, Fe_2O_3, and TiO_2, as expected for marble-related rocks. By comparing the investigated samples and those of Balassone et al. (2013), the skarn samples have similar values (Fig. S1). As already pointed out by Jolis et al. (2015), Somma-Vesuvius skarns typically have a large compositional range in terms of major elements, owing to the occurrence of variable silicates-oxides-carbonates assemblages (with different amounts of clinopyroxene, phlogopite, olivine, humites, spinel, calcite, etc.). In particular, the investigated Pompeii and Avellino skarn xenoliths and Pompeii composite skarn-marble plot between the marble xenoliths and the igneous

compositions in Jolis et al. (2015) (Fig. 4), depicting a continuous array; a similar trend can be pointed out in various Harker's diagrams (Fig. S1). The lack of systematic trend for MgO against SiO_2 suggests a combination of limestone and dolostone protoliths (Jolis et al., 2015).

Cumulate sample PS80 is quite close to the cumulate samples of Balassone et al. (2013) in terms of K_2O, Na_2O, Al_2O_3, Fe_2O_3 vs. SiO_2 and CaO correlations, whereas sample PS81 plots behaves differently (Fig. S1); it is worth noting that none of the Pompeii cumulates from this study display the high TiO_2 amount of up to 1.9 wt% (Fig. S1 f) in the AD 1944 eruption cumulates recorded by Balassone et al. (2013).

Syenite sample PS57 is characterized by high values of Al_2O_3 (20.1 wt%) and alkalis (9.76 wt% K_2O and 4.58 wt% Na_2O), as reported in Fig. S1a,b,c. In any case, cumulate and syenite ejecta display a narrow range of major oxide composition that plots in the intermediate position of the trend depicted by the entire sample set (Fig. 4; Fig. S1).

Whole-rock trace element concentrations are reported in Table 2 and a selection of elements is plotted against CaO wt% in Fig. S2. Trace element arrays are scattered for the skarn and composite skarn-marble samples, similarly to literature data. Broadly negative trends can be observed for Ba (with higher values for Pompeii composite sample PS40 and Avellino skarns PS60 and PS84), Zr (except to skarns PS55, Avellino, and PS82, Pompeii), Rb, Nb, V, Cs, and Tl when plotted against CaO (Fig. S2 a-h). The higher Sr concentrations are detected in some skarn-marble samples (PS44, PS62, and PS65, Pompeii), usually associated with the occurrence of calcite in the mineral assemblage (Fig. S2b). The Th values are commonly lower than 6 ppm, while it is higher in the skarn samples PS70 and PS73 (Avellino) and PS68 and PS77 (Pompeii) (Fig. S2i), without correlation with Th phases (Table 1). The concentrations of Cr, Ni, and Co are commonly low in the skarn samples (Table 1). Among base metals, Cu is very low, excepting for some Avellino samples (i.e., up to 40 ppm in PS55); Zn concentrations from 110 ppm to 660 ppm in Avellino skarn PS58 (Table 1), and Pb in the range <5-30 ppm up to 240 ppm in Pompeii skarn-marble PS44 are measured.

Cumulate samples PS80 and PS81 have low amounts of Ba, Sr, Zr, and Th, while sample PS81 has higher concentrations of Rb, V, Nb, Cs, and Tl compared to both all other xenoliths (Fig. S1c, d, f, g, h) and cumulate nodule in Balassone et al. (2013).

The Pompeii syenite PS57 generally have low concentrations of trace elements, except for Rb, Cs, and Tl amounts, which are closer to the cumulate samples.

The chondrite-normalized REE patterns shown in Fig. 5a display an enrichment in LREE (light rare earth elements: La, Ce, Pr, Nd) and MREE (medium rare earth elements: Sm, Eu, Gd, Tb, Dy) relative to HREE (heavy rare earth elements: Ho, Er, Tm, Yb, Lu), with a nearly flat pattern for HREE. These patterns follow the trend those of recent activity ejecta of Balassone et al. (2013, see Fig. 5a), with a wider variation in the LREE values; moreover, the positive Gd anomaly found in the cumulate sample of these authors was not detected in the Pompeii cumulates from the present study. Moreover, the composite skarn-marbles are more depleted in REE respect to most of the samples.

In the multi-elemental patterns (Fig. 5b), some elements such as Ba and Ta have a deep trough for all samples; a similar behavior is observed in most of samples for Th, Sr, P, and Ti, with some exceptions represented by skarns and/or composite rocks. A strongly Pb enrichment is observed in composite sample PS44 (Pompeii), whereas Pompeii skarn PS82 is characterized by higher concentrations of U and REE. Compared to the data of Balassone et al. (2013), a similar trace elements trend can be pointed out; higher concentrations of Ba, P, Eu, Tb, Y, Tm, and Yb of the AD 1944 cumulate of the cited authors are observed in comparison with the Pompeii cumulates of this work.

Micas

Mica crystals are commonly light green in color in skarn ejecta and composite rocks, whereas they have variable color from dark green to brown in the cumulates and syenite. Via SEM

observation, the micas habit is mainly euhedral, and clusters of hexagonal platy crystals are common. Micas can be found as laminae reaching up to 1 mm in length in cumulate and syenite samples, whilst smaller size of tens or few hundreds of µm can be detected in the marbles and skarns (Fig. 6).

Chemical composition

In the classification diagram *feal* against *mgli* (Fig. 7a), the Pompeii and Avellino micas fall within the compositional field of phlogopite[1]. They also define a linear trend between $^{[VI]}$Al-rich and Mg-poor "end-member", represented by PS68 (Avellino skarn), and a group of micas characterized by low $^{[VI]}$Al and high Mg contents, mainly belonging to Pompeii composite xenoliths. In the central part of this array, PS57 (Avellino syenite) and PS80 and PS81 (Pompeii cumulates) crystals are found. A similar trend was also observed for Vesuvian micas from Balassone et al. (2013), with $^{[VI]}$Al-rich and Mg-poor biotite from cumulate (AD 1944) on one side and micas from skarn (AD 1631) on the opposite site. The Si vs. Al content in tetrahedral site is nearly close to 4 apfu (atoms per formula unit; Fig. 7b), suggesting negligible $^{[IV]}Fe^{3+}$ occupancy in this site ($^{[IV]}Fe^{3+}$ = 0-0.07 apfu); also, the general decrease of the total content of Al with increasing Si (Table 3 and Fig. 7b) is compatible with an Al^{3+}-Tschermak substitution.

Using the tetrahedral diagram reporting the main octahedral Ti and $^{[VI]}$Al cations compared with F and Mg# (Fig. 8a), it is possible to observe that the skarn-related Avellino phlogopites can reach lower Mg#/2 values (up to 0.78, sample PS68) and higher $^{[VI]}$Al (up to 0.25 apfu, sample PS55) and Ti (up to 0.15 apfu, sample PS68) values compared to skarn- and composite rocks-deriving Pompeii phlogopite (see also Fig. S3a, b). The fluorine amounts vary in the interval 0.09-0.71 apfu for the Avellino phlogopite from skarn and in a slightly higher range (0-0.79 apfu) for micas of Pompeii metamorphic-metasomatic samples (Fig. 8a and Fig. S3c). Regarding the Pompeii cumulates, micas PS80 and PS81 have the highest $^{[VI]}$Al (up to 0.27 apfu) and F (up to 0.85 apfu)

[1] Possible lithium amounts, not analyzed in this study, may be considered negligible for the classification in the diagram of Fig, 7a.

values, respectively, of the whole analyzed samples (Table 3). Mica from Avellino syenite lies approximately between the fields of skarn/composite rocks dataset from the two eruptions (Fig. 8a and Fig. S3). Micas from Avellino skarns and Pompeii cumulates mainly have higher iron contents compared to the other samples (Fig. 8b), as also resulting from bulk-rock geochemistry (Fig. S1). Moreover, most of the investigated micas have a negligible "brittle mica component", due to a Ba amount lower than 0.005 apfu, except for micas from Avellino skarns PS60, PS84, and PSK-R which display Ba amounts in the interval 0.02-0.03 apfu (Fig. S4; Table 3).

In Fig. 8, the comparison between micas from the present study and those from recent activity of Vesuvius (Balassone et al., 2013) emphasizes that micas from AD 1631 skarns appear slightly closer than those from Pompeii eruption (Fig. S3 and S4); micas from pyrometamorphic/hydrothermally altered ejecta of AD 1872 are chemically rather different (as exemplified by higher F concentrations), and also mica from cumulate of AD 1944 eruption do not fit with samples from Pompeii cumulates from this study.

The substitution of Ba for K is mostly accounted for the coupled substitution $^{[XII]}Ba + {}^{[IV]}Al \leftrightarrow Si + {}^{[XII]}K$ (Fig. 9), with a linear array and end-members represented by PSK-R (Avellino skarn) and PS44 (Pompeii composite nodule) micas. A similar trend can be observed for Vesuvius micas from the most recent volcanic activity (Balassone et al., 2013). It is worth noting that in few Avellino and Pompeii micas small amounts of Sr (0.02-0.03 apfu) were detected (see samples PS41, PS60, PS84, and PSK-R in Table 3).

Plotted in the Al_2O_3 vs. TiO_2 and FeO_t (wt%) diagrams (Fig. 10a, b), the chemical feature of the studied micas from skarns and composite rocks fits most of those from the Vesuvian skarns (mainly Avellino, Pompeii, and AD 472 Pollena eruptions) of Gilg et al. (2001) in terms of Al_2O_3 and TiO_2, whereas have different values compared to micas in various xenoliths (lavas, metamorphic nodules, and composite rocks) from AD 1872 ejecta (Petti et al., 2010). The concentrations of FeO_t (wt%) and to some extent of the Mg# values of micas from skarn of Avellino and Pompeii (Fig. 10c) eruptions, variously different from the other studied micas (see also Fig.

8b), likewise differ from the other literature data. The FeO_t content is higher in Avellino than in Pompeii micas.

Crystallographic features

Mica crystals representative of the two clusters in the skarn and composite skarn-marble lithotypes identified based on the classification plot in Fig. 7 were selected for a deeper investigation by means of SCXRD. Unfortunately, it was not possible to obtain good-quality crystals for SCXRD investigations both from the syenite and cumulates.

Crystals from samples PS68 and PS77 (Avellino skarns) which exhibit slightly low Mg# as well as crystal from PS50, PS62, and PS73 (Pompeii composite skarns-marbles and skarns) with high Mg# were deeper analyzed. The results of the structure refinements converged to good values of the agreement indexes, $R_1 \leq 3.29$ % and $wR_2 \leq 4.98$ %. All samples are 1*M* polytypes and crystallize in the *C*2/*m* space group, except for the PS77 which was refined in *C*2 space group (Table 4). The PS50 crystal resulted to be twinned with 0.67(2):0.271(9) refined proportion between the two individuals. The samples have a great variability of the lattice constants, especially of the *c* axis [$5.3055(1) \leq a \leq 5.3218(1)$ Å, $9.1893(1) \leq b \leq 9.2188(4)$ Å, $10.1803(2) \leq c \leq 10.2951(2)$ Å]. The PS68 crystal has the shortest *c* cell parameters [10.1803(2) Å] which is typical of de-hydrogenated phlogopite (Lacalamita et al., 2011; Schingaro et al., 2011; Lacalamita et al., 2017). On the contrary PS50 and PS62 crystals from Pompeii have a *c* cell parameter [10.2932(4) and 10.2951(2) Å, respectively], which approximates that of the endmember phlogopite (Redhammer and Roth, 2002), in agreement with the trend in Fig. 7. Regarding the bond lengths (Table 5), almost all the studied samples are geometrically 'homo-octahedral' (i.e., <M1-O> equals the <M2-O> distance within three standard deviations, Weiss et al., 1992). Among the individual distances, the PS68 crystal has the M2-O4 bond length remarkably shorter with respect to the other two <M2-O3> distances (Table 5) which is one of the clues of the possible occurrence of oxy-type substitutions. Consistently, it also has the smallest cell volume (Table 4).

Crystal-chemistry

The structural formulae of the selected mica crystals are listed in Table 6. They were obtained by combining the results from the microprobe analysis (Table 3) and structure refinements (Tables 5 and 7), with estimated H_2O content (Ventruti et al., 2008) following the approach reported elsewhere (see for instance Schingaro et al., 2012; Lacalamita et al., 2017).

The formulae are balanced based on the main substitutions: M^{3+}-Tschermak [$^{VI}M^{2+} + {}^{IV}Si^{4+} \leftrightarrow {}^{VI}(Al^{3+}, Fe^{3+}) + {}^{IV}Al^{3+}$]; Ti-oxy [$^{VI}M^{2+} + 2(OH)^{-} \rightarrow {}^{VI}Ti^{4+} + 2(O)^{2-} + H_2\uparrow$]; M^{3+}-oxy [$^{VI}M^{2+} + (OH)^{-} \leftrightarrow {}^{VI}M^{3+} + O^{2-} + ½ H_2$]; $OH^{-} \rightarrow F^{-}$. The tetraferriphlogopite [$^{IV}Fe^{3+} \leftrightarrow {}^{IV}Al$] substitution also characterizes the PS73 mica.

Fig. 11 exhibits the variation of the *c* cell parameter versus the Mg number [$Mg/(Mg+Fe_{tot})$]. The highest values of the Mg number pertain to the OH-rich phlogopite (PS50 and PS62 Pompeii samples), as well as fluorophlogopite from the AD 1872 eruption of Vesuvius. The latter exhibits *c* shortening typical of dehydrogenation (see below). For the remaining crystals, as well as for other phlogopite and biotite from Vesuvius xenoliths (Balassone et al., 2013), the *c* parameter decreases with the increase of the Fe content, that, alone or with other metals, may be involved in oxy-type substitution in micas.

In the case of the more dehydrated (see section above) PS68 crystal, the entry of Ti and M^{3+} cations in the octahedral site by oxy-mechanism involving the deprotonation process at the anionic O4 site, strongly affects the values of geometrical parameters (short *c* cell parameter, M2-O4 and K-O4 distances; high values of M2 bond lengths distortion, BLD_{M2}; strong displacement, $shift_{M2}$, of the M2 octahedral cation from the geometric center of the octahedron, etc., see Tables 4 and 5) which are consistent with those found for Ti-oxy phlogopite (Cruciani and Zanazzi, 1994). On the contrary, the very low extent of oxy-mechanisms and $OH^{-} \rightarrow F^{-}$ replacement in PS50 and PS62 end-member crystals explains the high values of the *c* cell parameter and the low values of the BLD_{M2} and $shif_{M2}$ parameters (Table 5). For these crystals, the high charge cations are equally

distributed between the M1 and M2 octahedral sites as testified by the very close values of the <M1-O> and <M2-O> distances and volumes of the octahedra (Table 5). These crystals also have the highest value (~11° vs 9°, Table 5) of the tetrahedral rotation angle, α, with respect to the other studied crystals. This parameter describes the in-plane rotation of adjacent tetrahedra in opposite directions respect with c*. The large α parameter of PS50 and PS62 crystals indicate a good congruence between the tetrahedral and octahedral sheet.

The PS77 and PS73 samples exhibit the same degree of dehydrogenation (O^{2-}+F^{-} content ~ 0.8 apfu) resulting in a *c* cell parameter (~10.23 Å, Table 4) intermediate between those of dehydrogenated (PS68 sample) and OH-rich phlogopite (PS50 and PS62 samples). The high charge cation at the octahedral sites is essentially involved in M^{3+}-Tschermak substitutions (Table 6). In the case of the PS73 crystal, the best structural formula was obtained by considering the total iron as Fe_2O_3 which was distributed between both the octahedral and tetrahedral sites.

In the $Shift_{M2}$ parameter against Ti and F (Fig. S5a) four points fall close to the AD 1631 literature data and define a slightly flat pattern, whereas a particularly high Ti and $Shift_{M2}$ values for the mica from Avellino skarn PS68 can be observed. Also in the $Shift_{M2}$ vs. F (apfu) diagram (Fig. S5b) sample PS68 plots as an outlier, due to its high value of $Shift_{M2}$, while the other samples behave as in Fig. S5a. Fig. S5c, d shows the in-plane rotation angle, i.e., α parameter (°), as a function of the Ti and F contents; in the α vs. Ti diagram (Fig. S5c) micas from the Pompeii skarn-marble samples PS50 and PS62 and from the skarn PS77, as well as the Avellino skarn PS73, are closer to the literature AD 1631 samples, whereas mica from the Avellino skarn PS68 plots very close to micas from the AD 1944. In the α vs. F plot of Fig. S5d a broad negative trend is observed, with the investigated micas close to the AD 1631 and AD 1944 data.

Crystallization conditions

Considering the mineralogical assemblages observed in most xenoliths, indicative of crystallization conditions during their formation, and following Guarino and Brigatti (2018, and references therein), we try to estimate the crystallization temperature at which the micas are formed. Using the geothermometer of Luhr et al. (1984) [T (K) = 838/(1.0337 – Ti/Fe^{2+})] based on the ratio between octahedral Ti and Fe^{2+}, we have obtained similar ranges of temperatures, i.e., 541 - 583 °C and 545 - 596°C for the Pompeii and Avellino xenoliths (Table 3). A higher temperature (824 °C) was obtained for mica in skarn PS68, due to its high Ti/Fe^{2+} ratio. For the Pompeii composite sample PS62, the Ti/Fe^{2+} value of 0.54 made the above formula inapplicable.

The formula proposed by Uchida et al. (2007) for pressure determination cannot be applied because the studied micas have the total aluminum less than 1.5 apfu.

We tested other thermobarometers based on different mineral pairs, as apatite-phlogopite (Ludington, 1978; Seifert et al., 2000), garnet-clinopyroxene (Duchêne and Albarède, 1999) and garnet-biotite (Reche and Martinez 1996; Wu, 2015), but unreliable results were obtained because the minerals/rocks are commonly not in equilibrium.

IMPLICATIONS

The mineralogical features and genetic inferences of the studied mica-bearing ejecta may provide valuable information for reconstructing the environmental conditions at Somma-Vesuvius and in similar geological systems.

Firstly, the crystal chemical analysis of micas from different xenoliths related to Avellino and Pompeii Plinian eruptions of Somma-Vesuvius volcano evidenced that they belong to the phlogopite-annite join. They are affected by different cations substitutions and dehydrogenation degrees, that largely extend the known range of the other Vesuvian micas (as in Balassone et al., 2013), providing some genetic indications, that can be of certain utility also for the understanding

the quiescent volcano dynamics. Their host rocks have a wide composition reflecting the abundance of carbonate or silicate phases (i.e., CaO richer Pompeii skarns-to-marbles or SiO_2 enriched Avellino ejecta, respectively). The main mineralogical and petrological aspects can be summarized as follows:

Micas from skarns and composite skarn-marble rocks. The studied Avellino and Pompeii phlogopites from skarns and composite skarn-marbles are generally Ti-depleted, as also found in most of phlogopites from Avellino, Pompeii, and Pollena of Gilg et al. (2001), and slightly more Ti-depleted than the AD 1631 micas of Balassone et al. (2013). Concurrently, they have variable amounts of Al and F, in keeping with the compositional ranges reported by the cited literature. However, the micas set of the present work (i.e., both samples of metamorphic/metasomatic and of igneous origin) never reach the high F concentrations detected in micas in AD 1872 xenoliths (Balassone et al., 2013), which correspond to fluorophlogopite composition and testify for a strongly dehydrated condition. Similarly, the studied phlogopites display chemical characteristics significantly different from the micas batch related to the AD 1872 nodules of Petti et al. (2010). These AD 1872 xenoliths are pyrometamorphic/hydrothermally altered nodules explaining the very different nature and crystallization conditions of micas.

In terms of Mg# and Fe, the micas of this study are more variable compared to the previously cited literature data; in particular, three samples from skarn of Avellino eruption, i.e., PS55, PS68, and PS77, have higher Fe contents and lower Mg# values. Interestingly, mica PS68 is also distinctly highest in Ti concentration of the whole sample set, accompanied by a lower *c* parameter; concurrently, the host rock is Fe-rich and have quite high MgO and TiO_2 values, in relation with silicate-oxide (mica+clinopyroxene+magnetite+vesuvianite) mineral assemblage. According to Laurora et al. (2007), micas with the highest Ti contents can be ideally in equilibrium with a more-evolved melt enriched in Fe and Ti.

The chemical and structural data indicate that micas PS73 (Pompeii) and PS77 (Avellino) samples exhibit the same degree of dehydrogenation, resulting in a *c* cell parameter intermediate between those of dehydrogenated (PS68 sample; Avellino) and OH-rich phlogopite (P50 and PS62 Pompeii samples). It appears that the phlogopite dehydrogenation variability is higher in ejecta from highest VEI Pompeii eruptions, whereas it is more clustered in those from the AD 1631 and 1944 eruptive events. Highly dehydrated mica structure coupled with a fluorophlogopite composition found in AD 1872 ejecta (Balassone et al., 2013), characterized by lower P and higher T environment, have never been found in the present study. Following their reasoning, more variable pressure conditions should be consistent with the environment of fluid-carbonate wall rock interaction developed around the Pompeii and Avellino magma chambers.

Concerning the temperatures, fluid inclusion studies of Gilg et al. (2001) give a range of 800-890 °C for most skarn-derived minerals (vesuvianite, calcite) indicating initial temperatures related to the entrapment of these fluid inclusions during crystal growth, similarly was obtained for mica in sample PS68 (824 °C). Differently the generally low temperatures estimated for micas in the skarns and composite skarn-marbles (541-596 °C) well represent the minimum crystallization temperatures related to contact metamorphism.

This can be supported by the presence of humite, suggesting that dehydrated micas can occur under high CO_2/H_2O (and F) conditions during their growth by contact metamorphism with with carbonatic limestones. As proposed by Young and Morrison (1992), the humite features of our samples would result by devolatilization reactions driven by addition of aqueous fluid and extraction of heat in endoskarn around plutons at less than 600°C. The presence of humite species in the ejecta paragenesis deserves further studies in order to evaluate stable isotope shift in skarn's calcite correlated with its growth proposed by the Authors.

As concerns the Ba content, it is worth noting that micas from Avellino skarn PS60, PS84, and PSK-R have higher Ba amounts compared to the other samples; at the same time, the related host rocks PS60 and PS84 also has the highest Ba concentrations, even though this correlation does

not occur for PSK-R sample. Finally, the higher Sr concentrations detected in three of the Pompeii skarn-marble nodules are not reflected in micas composition.

Unlike Pompeii, Avellino magmas were usually leucite-free. Leucite in Avellino skarns could suggest that the K enrichment already occurred in the Vesuvius magmatism before the AD 79, either as a primary magma feature or as an effect of carbonate assimilation (Piochi et al., 2006a; Mollo et al., 2010).

All the skarns and skarn-marbles contain several F-bearing minerals supporting the role of "fluorine-bearing aqueous-carbonic fluids" in the magma-host rock processes suggested in previous studies (Gilg et al., 2001 and references therein).

Micas from cumulates and syenite. Micas related to cumulates (Pompeii eruption) are compositionally different from cumulate sample from the AD 1944 eruption of Balassone et al. (2013); they are distinctly more depleted in Fe, Ti and Ba and enriched in F and Mg, whereas the Al concentration is variable.

Mica from syenite (Avellino eruption) appears to record similar low to medium concentrations of selected elements detected in the source rock, as Ti, Ba, Mg, and Fe.

Syenite and one cumulate xenolith have the highest content of Cs and Rb, as expected from the major role of the magmatic processes. The low content of crystallizing mica mainly in syenite can determine the observed enrichment of Cs and Rb. This can be associated with pressure conditions exceeding the mica stability, i.e., depth shallower than 4 km (Fabbrizio and Carroll, 2008; Scaillet et al., 2001). Similar minimum crystallization temperatures related to contact metamorphism are also obtained for micas in syenite (554 °C) and and other skarn to cumulate xenoliths (558-583 °C).

Remarkably, sodalite is common in Avellino and not in Pompeii magmas (Piochi et al., 2006a and references therein). Its occurrence in the Pompeii cumulate should be associated with an Avellino's remnant thrown out by the AD 79 eruption.

Finally, this study highlights the importance of micas crystal chemical features in the genetic contexts.

As stated by Lepore et al. (2017), commonly petrologists use only microprobe data and petrographic details to classify mica and the formula is derived by placing the obtained chemical data in worksheets. Often, to get charge neutrality, fanciful cation distributions are hypothezised (e.g., Mg in the tetrahedral site), neglecting crucial information like the role of the light elements (including a possible dehydrogenation) and a good estimation of the Fe^{2+}/Fe^{3+} ratio. Indeed, both the estimation of the Fe^{2+}/Fe^{3+} ratio and the quantification of light elements (H and Li) are also key variables to obtain insights on the relationship between the studied phase and the crystallization conditions.

In the case of absence of direct estimation of the above variables the crystal chemical details may be of help: the hydrogen content can be estimated from the c parameter and the Fe^{2+}/Fe^{3+} ratio the one providing the best agreement between the EPMA-derived and the structure refinement-derived mean atomic numbers as well as between calculated and observe bond distances (Ottolini et al., 2012). Structural evidence (i.e., geometrical distortions) of substitution mechanisms can also be employed. This alternative approach is indeed widely recognized and has been pursued in the present work.

ACKNOWLEDGEMENTS

This work is dedicated to the memory of Prof. Enrico Franco, who introduced GB to the study of the Somma-Vesuvius minerals and donated her his personal collection of Vesuvian specimens. We are grateful to Warren Huff for helpful suggestions and for the editorial handling of the manuscript. The revision of Alex Asavin and an anonymous reviewer provided us useful insights

that greatly enhanced the quality of the paper. Roberto de Gennaro (DiSTAR, Naples) and Marcello Serracino (IGAG CNR, Rome) are thanked for some SEM-EDS and WDS analyses, respectively. This study was supported by the research funds 'Ricerca Dipartimentale 2016-2017' from the Dipartimento di Scienze della Terra, dell' Ambiente e delle Risorse of the Università degli Studi di Napoli Federico II (Italy) granted to GB. VULCAMED and EPOS Research Infrastructure through the contribution of the Italian Ministry of University and Research (MUR) provided financially supports to Istituto Nazionale di Geofisica e Vulcanologia for the X-ray diffraction laboratory at the Osservatorio Vesuviano.

REFERENCES CITED LIST

Abrecht, J., and Hewitt, D.A., (1988) Experimental evidence on the substitution of Ti in biotite. American Mineralogist, 73, 1275-1284.

Arrighi, S., Principe, C., and Rosi, M. (2001) Violent strombolian and subplinian eruptions at Vesuvius during post-1631 activity. Bulletin of Volcanology, 63, 126-150.

Auger, E., Gasparini, P., Virieux, J., and Zollo, A. (2001) Seismic evidence of an extended magmatic sill under Mt. Vesuvius. Science, 294, 1510-1512, doi:10.1126/science.1064893.

Avanzinelli, R., Cioni, R., Conticelli, S., Giordano, G., Isaia, R., Mattei, M., Melluso, L., and Sulpizio R. (2017) The Vesuvius and the other Volcanoes of Central Italy. Geological Field Trips 9(1.1), http://www.isprambiente, gov.it/it/pubblicazioni/periodici-tecnici/geological-field-trips [accessed on 5 January 2021].

Ayuso, R.A., Vivo, B.D., Rolandi, G., and Paone, A. (1998) Geochemical and isotopic (Nd–Pb–Sr–O) variations bearing on the genesis of volcanic rocks from Vesuvius, Italy. Journal of Volcanology and Geothermal Research, 82, 53-78.

Babushkina, M.S., Lepekhina, E.N., Nikitina, L.P., Ovchinnikov, N.O., and Lokhov, K.I. (2000) Crystal structure defects of micas from lamproites (Mossbauer and infrared spectroscopy data). Doklady Akademii Nauk, 371, 797-801 (in Russian).

Balassone, G., Bellatreccia, F., Mormone, A., Biagioni, C., Pasero, M., Petti, C., Mondillo, N., and Fameli, G. (2012) Sodalite-group minerals from the Somma-Vesuvius volcanic complex, Italy: a case study of K-feldspar-rich xenoliths. Mineralogical Magazine, 76, 191-212.

Balassone, G., Scordari, F., Lacalamita, M., Schingaro, E., Mormone, A., Piochi, M., Petti C., and Mondillo N. (2013) Trioctahedral micas in xenolithic ejecta from recent volcanism of the Somma-Vesuvius (Italy): Crystal chemistry and genetic inferences. Lithos, 160-161, 84-97.

Balassone, G., Bellatreccia, F., Ottolini, L., Mormone, A., Petti, C., Ghiara, M.R., Altomare, A., Saviano, M., Rizzi, R., and D'Orazio L. (2016) Sodalite-group minerals from Somma-Vesuvius volcano (Naples, Italy): A combined EPMA, SIMS and FTIR crystal chemical study. The Canadian Mineralogist, 54, 583-604, doi.10.3749/canmin.1500083.

Balcone-Boissard, H., Boudon, G., Ucciani, G., Villemant, B., Cioni, R., Civetta, L., and Orsi, G. (2012) Magma degassing and eruption dynamics of the Avellino pumice Plinian eruption of Somma–Vesuvius (Italy). Comparison with the Pompeii eruption. Earth and Planetary Science Letters, 331-332, 257-268.

Barberi, F., and Leoni, L. (1980) Metamorphic carbonate ejecta from Vesuvius Plinian eruptions: evidence of the occurrence of shallow magma chambers. Bulletin of Volcanology, 43, 107-120.

Barberi, F., Bizouard, H., Clocchiatti, R., Metrich, N., Santacroce, R., and Sbrana, A. (1981). The Somma-Vesuvius magma chamber: a petrological and volcanological approach. Bulletin Volcanologique, 44, 295-315.

Betteridge, P.W., Carruthers, J.R., Cooper, R.I., Prout, K., and Watkin, D.J. (2003) Crystals version: software for guided crystal structure analysis. Journal of Applied Crystallography, 36, 1487.

Brigatti, M.F., Galli, E., and Poppi, L. (1991) Effect of Ti substitution in biotite-1*M* crystal chemistry. American Mineralogist, 76, 1174-1183.

Brigatti, M.F., and Poppi, L. (1993) Crystal chemistry of Ba-rich trioctahedral micas-1*M*. European Journal of Mineralogy, 5, 857–871.

Brigatti, M.F., Caprilli, E., Funiciello, R., Giordano, G., Mottana, A., and Poppi, L. (2005) Crystal chemistry of ferroan phlogopites from the Albano maar lake zone (Colli Albani volcano, central Italy). European Journal of Mineralogy, 17, 611-621.

Brocchini, D., Principe, C., Castradori, D., Laurenzi, M.A., and Gorla, L. (2001) Quaternary evolution of the southern sector of the Campanian Plain and early Somma-Vesuvius activity: insights from Trecase 1 well. Mineralogy and Petrology, 73, 67-91.

Bruno, P.P.G., Cippitelli, G., and Rapolla, A. (1998) Seismic study of the Mesozoic carbonate basement around Mt. Somma-Vesuvius, Italy. Journal of Volcanology and Geothermal Research, 84, 311-322.

Bruker (2007) SAINT, Bruker AXS Inc., Madison, Wisconsin, USA.

Bruker (2009) SADABS, Bruker AXS Inc., Madison, Wisconsin, USA.

Bruker (2010) APEX2 v.2010.7-0, Bruker AXS Inc., Madison, Wisconsin, USA.

Cioni, R., Civetta, L., Marianelli, P., Metrich, N., Santacroce, R., and Sbrana, A. (1995) Compositional layering and syn-eruptive mixing of a periodically refilled shallow magma chamber: the AD 79 Plinian eruption of Vesuvius. Journal of Petrology, 36, 739-776.

Cioni, R., Santacroce, R., and Sbrana, A. (1999) Pyroclastic deposits as a guide for reconstructing the multi-stage evolution of the Somma-Vesuvius Caldera. Bulletin of Volcanology, 60, 207-222.

Cioni, R. (2000) Volatile content and degassing processes in the AD 79 magma chamber at Vesuvius (Italy). Contribution to Mineralogy and Petrology, 140, 40-54.

Cioni, R., Bertagnini, A., Santacroce, R., and Andronico, D. (2008) Explosive activity and eruption scenarios at Somma-Vesuvius (Italy): Towards a new classification scheme. Journal of Volcanology and Geothermal Research, 178, 331-346.

Civetta, L., D'Antonio, M., de Lorenzo, S., Di Renzo, V., and Gasparini, P. (2004) Thermal and geochemical constraints on the 'deep' magmatic structure of Mt. Vesuvius. Journal of Volcanology and Geothermal Research, 133, 1-12.

Conticelli, S., Guarnieri, L., Farinelli, A., Mattei, M., Avanzinelli, R., Bianchini, G., Boari, E., Tommasini, S., Tiepolo, M., Prelević, D., and Venturelli, G. (2009) Trace elements and Sr–Nd–Pb isotopes of K-rich, shoshonitic, and calc-alkaline magmatism of the Western Mediterranean Region: genesis of ultrapotassic to calc-alkaline magmatic associations in a post-collisional geodynamic setting. Lithos, 107, 68-92.

Conticelli, S., Laurenzi, M.A., Giordano, G., Mattei, M., Avanzinelli, R., Melluso, L., Tommasini, S., Boari, E., Cifelli, F., and Perini, G. (2011) Leucite-bearing (kamafugitic/leucititic) and -free (lamproitic) ultrapotassic volcanic rocks and associated shoshonites in the Italian Peninsula: constraints on petrogenesis and geodynamics. In: "The Geology of Italy: tectonics and life along plate margins", Beltrando, M., Peccerillo, A., Mattei, M., Conticelli, S., Doglioni, C. (Eds.), Journal of the Virtual Explorer 36, paper 20, 1-95, https://dx.doi.org/10.3809/jvirtex.2009.00251.

Cruciani, G., and Zanazzi, P.F. (1994) Cation partitioning and substitution mechanisms in 1 M phlogopite: a crystal chemical study. American Mineralogist, 79, 289-301.

Cucciniello, C. (2016) Tetra-plot: a Microsoft Excel spreadsheet to perform tetrahedral diagrams. Periodico di Mineralogia, 85, 115-119.

Dallai, L., Cioni, R., Boschi, C., and D'Oriano, C. (2011) Carbonate-derived CO_2 purging magma at depth: Influence on the eruptive activity of Somma-Vesuvius, Italy. Earth and Planetary Science Letters, 310, 84-95.

Di Renzo, V., Di Vito, M.A., Arienzo, I., Civetta, L., D'Antonio, M., Giordano, F., Orsi, G., and Tonarini, S. (2007) Magmatic history of Somma-Vesuvius on the basis of new geochemical and isotopic data from a deep borehole (Camaldoli della Torre). Journal of Petrology, 48, 753-784.

Del Moro, A., Fulignati, P., Marianelli, P., and Sbrana, A. (2001) Magma contamination by direct wall rock interaction, constraints from xenoliths from the walls of a carbonate-hosted magma chamber (Vesuvius 1944 eruption). Journal of Volcanology and Geothermal Research, 112, 15-24.

Di Vito, M.A., Talamo, P., de Vita, S., Rucco, I., Zanchetta, G., and Cesarano, M. (2019) Dynamics and effects of the Vesuvius Pomici di Avellino Plinian eruption and related phenomena on the Bronze Age landscape of Campania region (Southern Italy). Quaternary International, 499, 231-244.

Doronzo, D.M., Di Vito, M.A., Arienzo, I., Bini, M., Calusi, B., Cerminara, M., Corradini, S., de Vita, S., Giaccio, B., Gurioli, L., Mannella, G., Ricciardi, G.P., Rucco, I., Sparice, D., Todesco, M., Trasatti, E., and Zanchetta, G. (2022) The 79 CE eruption of Vesuvius: A lesson from the past and the need of a multidisciplinary approach for developments in volcanology, Earth-Science Reviews, 231, 104072, doi.org/10.1016/j.earscirev.2022.104072.

Duchêne, S., and Albarède, F.(1999) Simulated garnet-clinopyroxene geothermometry of eclogites. Contributions to Mineralogy and Petrology, 135(1), 75.

Dymek, R.F. (1983) Titanium, aluminum and interlayer cation substitutions in biotite from high grade gneisses, West Greenland. American Mineralogist, 68, 880-899.

Fabbrizio, A., and Carroll, M.R. (2008) Experimental constraints on the differentiation process and pre-eruptive conditions in the magmatic system of Phlegraean Fields (Naples, Italy). Journal of Volcanology and Geothermal Research, 171, 88-102.

Fritschle, T., Prelević, D., Foley, S.F., and Jacob, D.E. (2013) Petrological characterization of the mantle source of Mediterranean lamproites: Indications from major and trace elements of phlogopite. Chemical Geology, 353, 267-279.

Fulignati, P., Panichi, C., Sbrana, A., Caliro, S., Gioncada, A., and Del Moro, A. (2005) Skarn formation at the walls of the 79AD magma chamber of Vesuvius (Italy): Mineralogical and isotopic constraints. Neues Jahrbuch fur Mineralogie, Abhandlungen 181/1.

Gilg, H.A., Lima, A., Somma, R., Belkin, H.E., De Vivo, B., and Ayuso, R.A. (2001) Isotope geochemistry and fluid inclusion study of skarns from Vesuvius. Mineralogy and Petrology, 73, 145-176.

Guarino, V., and Brigatti, M.F. (2018) Crystallization conditions of micas in oxidized igneous systems. American Mineralogist, 103, 1999-2010, doi: https://doi.org/10.2138/am-2018-6567.

Gurioli, L., Houghton, B.F., Cashman, K.V., and Cioni, R. (2005) Complex changes in eruption dynamics during the 79 AD eruption of Vesuvius. Bulletin of Volcanology, 67, 144-159, doi:10.1007/s00445-004-0368-4.

Iacono-Marziano, G., Gaillard, F., and Pichavant, M. (2008) Limestone assimilation by basaltic magmas: an experimental re-assessment and application to Italian volcanoes. Contributions to Mineralogy and Petrology, 155, 719-738, doi: 10.1007/s00410-007-0267-8.

Iacono-Marziano, G., Gaillard, F., Scaillet, B., Pichavant, M., and Chiodini, G. (2009) Role of non-mantle CO_2 in the dynamics of volcano degassing: The Mount Vesuvius example. Geology, 37, 319-322.

Jolis, E.M., Freda, C., Troll, V.R., Deegan, F.M., Blythe, L.S., McLeod, C.L., and Davidson, J.P., (2013) Experimental simulation of magma–carbonate interaction beneath Mt. Vesuvius, Italy. Contrib. Mineralogy and Petrology, 166, 1335-1353, http://dx.doi.org/10.1007/s00410-013-0931-0.

Jolis, E.M., Troll, V.R., Harris, C., Freda, C., Gaeta, M., Orsi, G., and Siebe, C. (2015) Skarn xenolith record crustal CO2 liberation during Pompeii and Pollena eruptions, Vesuvius volcanic system, central Italy. Chemical Geology, 415, 17-36.

Joron, J.L., Métrich, N., Rosi, M., Santacroce, R., and Sbrana, A. (1987) Chemistry and petrography. In: Santacroce, R. (Ed.), Somma-Vesuvius. Quaderni de "La Ricerca Scientifica" CNR: Roma, 8, 105-171.

Lacalamita, M., Schingaro, E., Scordari, F., Ventruti, G., Fabbrizio, A., and Pedrazzi, G. (2011) Substitution mechanisms and implications for the estimate of water fugacity for Ti-rich phlogopite from Mt. Vulture (Potenza, Italy). American Mineralogist, 96, 1381-1391.

Lacalamita, M., Mesto, E., Scordari, F., and Schingaro, E. (2012) Chemical and structural study of 1M-and 2M1-phlogopites coexisting in the same Kasenyi kamafugitic rock (SW Uganda). Physics and Chemistry of Minerals, 39, 601-611.

Lacalamita, M., Balassone, G., Schingaro, E., Mesto, E., Mormone, A., Piochi, M., Ventruti, G., and Joachimski, M. (2017) Fluorophlogopite-bearing and carbonate metamorphosed xenoliths from the Campanian Ignimbrite (Fiano, southern Italy): crystal chemical, geochemical and volcanological insights. Mineralogical Magazine, 81, 1165-1189.

Lacalamita, M., Schingaro, E., Mesto, E., Zaccarini, E., and Biagioni, C. (2020) Crystal-chemistry of micas belonging to the yangzhumingite-fluorophlogopite and phlogopite-fluorophlogopite series from the Apuan Alps (northern Tuscany, Italy). Physics and Chemistry of Minerals, 47, 54, 8-10.

Laurora, A., Brigatti, M.F., Mottana, A., Malferrari, D., and Caprilli, E. (2007) Crystal chemistry of trioctahedral micas in alkaline and subalkaline volcanic rocks: A case study from Mt. Sassetto (Tolfa district, Latium, central Italy). American Mineralogist, 92, 468-480.

Laurora, A., Malferrari, D., Brigatti, M.F., Mottana, A., Caprilli, E., Giordano, G., and Funiciello, R. (2009) Crystal chemistry of trioctahedral micas in the top sequences of the Colli Albani volcano, Roman Region, central Italy. Lithos, 113, 507-520.

Lepore, G.O., Bindi, L., Pedrazzi, G., Conticelli, S., and Bonazzi, P. (2017) Structural and chemical variations in phlogopite from lamproitic rocks of the Central Mediterranean region. Lithos, 286-287, 191-205.

Ludington, S. (1978) The biotite-apatite geothermometer revisited. American Mineralogist, 63(5-6), 551-553.

Luhr, J.F., Carmichael, I.S.E., and Varekamp, J.C. (1984) The 1982 eruptions of El Chichón Volcano, Chiapas, Mexico: Mineralogy and petrology of the anhydrite bearing pumices. Journal of Volcanology and Geothermal Research, 23(1-2), 39-68.

Lyubetskaya, T., and Korenaga, J. (2007) Chemical composition of Earth's primitive mantle and its variance: 1. Methods and results. Journal of Geophysical Research, 112, 1-21, B03211.

McDonough, W.F., and Sun, S.S. (1995) The composition of the Earth. Chemical Geology, 120, 223-253.

Marianelli, P., Metrich, N., and Sbrana, A. (1999) Shallow and deep reservoirs involved in magma supply of the 1944 eruption of Vesuvius. Bulletin of Volcanology, 61, 48-63.

Massaro, S., Costa, A., and Sulpizio, R. (2018) Evolution of the magma feeding system during a Plinian eruption: the case of Pomici di Avellino eruption of Somma-Vesuvius, Italy. Earth and Planetary Science Letters, 482, 545-555.

Matarrese, S., Schingaro, E., Scordari, F., Stoppa, F., Rosatelli, G., Pedrazzi, G., and Ottolini, L. (2008) Crystal chemistry of phlogopite from Vulture-S.Michele Subsynthem volcanic rocks (Mt. Vulture, Italy) and volcanological implications. American Mineralogist, 93, 426-437.

McDonough, W., and Sun, S.S. (1995) The composition of the Earth. Chemical Geology, 67, 1050-1056.

Melluso, L., Scarpati, C., Zanetti, A., Sparice, D., and de' Gennaro, R. (2022) The petrogenesis of chemically zoned, phonolitic, Plinian and sub-Plinian eruptions of Somma-Vesuvius, Italy: role of accessory phase removal, independently filled magma reservoirs with time, and

transition from slightly to highly silica undersaturated magmatic series in an ultrapotassic stratovolcano. Lithos, 430, 106854.

Mollo, S., Gaeta, M., Freda, C., Di Rocco, T., Misiti, V., and Scarlato, P. (2010) Carbonate assimilation in magmas: a reappraisal based on experimental petrology. Lithos, 114(3-4), 503-514.

Mormone, A., Piochi, M., Balassone, G., Carlino, S., Somma, R., Troise, C., and De Natale, G. (2014) Mineralogical and petrological investigations of rocks cored from depths higher than 440 m during the CFDDP drilling activities at the Campi Flegrei caldera (southern Italy). In EGU General Assembly Conference Abstracts (p. 14198).

Moretti, R., Arienzo, I., Civetta, L., Orsi, G., and Papale, P. (2013) Multiple magma degassing sources at an explosive volcano. Earth and Planetary Science Letters, 367, 95-104.

Ottolini, L.P., Schingaro, E., and Scordari, F. (2012) Ceramics: contribution of secondary ion mass spectrometry (SIMS) to the study of the crystal chemistry of mica minerals. Mass Spectrometry Handbook, Mike S. Lee Editor, Wiley, pp.1017-1059.

Pappalardo, L., Piochi, M., and Mastrolorenzo, G. (2004) The 3550 year BP-1944 A.D. magma-plumbing system of Somma-Vesuvius: constraints on its behaviour and present state through a review of Sr-Nd isotope data. Annals Geophysics, 47, 1471-1483.

Pascal, M.-L., Di Muro, A., Fonteilles, M., and Principe, C. (2009) Zirconolite and calzirtite in banded forsterite-spinel-calcite skarn ejecta from the 1631 eruption of Vesuvius: inferences for magma-wallrock interactions. Mineralogical Magazine, 73(2), 333–356.

Pascal, M.L., Fonteilles, M., Boudouma, O., and Principe, C. (2011) Qandilite from Vesuvius skarn ejecta: Conditions of formation and miscibility gap in the ternary spinel–qandilite–magnesioferrite. The Canadian Mineralogist, 49, 459-485.

Peccerillo, A. (2005) Plio-Quaternary Volcanism in Italy. Petrology, Geochemistry, Geodynamics. Springer Berlin Heidelberg, New York, pp. 365.

Petti, C., Balassone, G., Bernardi, A.M., Mormone, A., Rossi, M., and Ghiara, M.R. (2010) Ejected rocks from the 1872 eruption of Vesuvius, Italy: a petrographic and mineralogical overview. Periodico di Mineralogia, 79, 1-25.

Pichavant, M., Scaillet, B., Pommier, A., Iacono-Marziano, G., and Cioni, R. (2014) Nature and evolution of primitive Vesuvius magmas: an experimental study. Journal of Petrology, 55, 2281-2310.

Piochi, M., Pappalardo, L., and De Astis, G. (2004) Geochemical and isotopical variations within the Campanian Comagmatic Province: implications on magma source composition. Annals of Geophysics 44, 1485-1499.

Piochi, M., Ayuso, R.A., De Vivo, B., and Somma, R. (2006a) Crustal contamination and crystal entrapment during polybaric magma evolution at Mt. Somma-Vesuvius volcano, Italy. Geochemical and Sr isotope evidence. Lithos, 86, 303-329.

Piochi, M., De Vivo, B., Ayuso, and R.A. (2006b) The magma feeding system of Somma-Vesuvius (Italy) strato-volcano: new inferences from a review of geochemical and Sr, Nd, Pb and O isotope data. Developments in Volcanology, 9, 181-202.

Pouchou, J.L., and Pichoir, F. (1991) Quantitative analysis of homogeneous or stratified microvolumes applying the model "PAP". In Electron probe quantitation, Springer, Boston, MA, pp. 31-75.

Reche, J., and Martinez, F. J. (1996) GPT: an Excel spreadsheet for thermobarometric calculations in metapelitic rocks. Computers & Geosciences, 22(7), 775-784.

Redhammer, G.J., and Roth, G. (2002) Single-crystal structure refinements and crystal chemistry of synthetic trioctahedral micas $KM_3(Al^{3+}, Si^{4+})_4O_{10}(OH)_2$, where M= Ni^{2+}, Mg^{2+}, Co^{2+}, Fe^{2+}, or Al^{3+}. American Mineralogist, 87, 1464-1476.

Rice, J.M. (1980) Phase equilibria involving humite minerals in impure dolomitic limestones, Part I. Calculated stability of clinohumite. Contributions to Mineralogy and Petrology 71, 219-235.

Russo, M., and Punzo, I. (2004) I minerali del Somma-Vesuvio. Associazione Mineralogica Italiana, Cremona, pp. 317.

Santacroce, R. (1987) Somma–Vesuvius. Quaderni della Recerca Scientifica CNR 114,pp. 1-230.

Santacroce, R., Cioni, R., Marianelli, P., Sbrana, A., Sulpizio, R., Zanchetta, G., Donahue, D.J., Joron, J.-L., 2008. Age and whole rock-glass composition of proximal pyroclastics from the major explosive eruptions of Somma–Vesuvius: a review as a tool for distal tephrostratigraphy. Journal of Volcanology and Geothermal Research, 177, 1-18.

Scaillet, B., Pichavant, M., Cioni, R., Sbrana, A., and Marianelli, P. (2001) Experimental constraints on pre-eruption conditions of plinian events at Vesuvius. In Geophysical Research Abstracts. EGU.

Scaillet, B., Pichavant, M., and Cioni, R. (2008) Upward migration of Vesuvius magma chamber over the past 20.000 years. Nature, 455, 216–219.

Schingaro, E., Kullerud, K., Lacalamita, M., Mesto, E., Scordari, F., Zozulya, D., Erambert, M., and Ravna, E.J. (2014) Yangzhumingite and phlogopite from the Kvaløya lamproite (North Norway): Structure, composition and origin. Lithos, 210-211, 1-13.

Schingaro, E., Lacalamita, M., Scordari, F., Brigatti, M.F., and Pedrazzi, G. (2011) Crystal chemistry of Ti-rich fluorophlogopite from Presidente Olegario, Alto Paranaíba igneous province, Brazil. American Mineralogist, 96, 732-743.

Schingaro, E., Scordari, F., and Ventruti, G. (2001) trioctahedral micas-1M from Mt. Vulture (Italy): Structural disorder and crystal chemistry. European Journal of Mineralogy 13, 1057-1069.

Scordari, F., Schingaro, E., Lacalamita, and M., Mesto, E. (2012. Crystal chemistry of trioctahedral micas-2M1 from Bunyaruguru (SW Uganda) kamafugite. American Mineralogist, 97, 430-439.

Seifert, W., Kämpf, H., and Wasternack, J. (2000) Compositional variation in apatite, phlogopite and other accessory minerals of the ultramafic Delitzsch complex, Germany: implication for cooling history of carbonatites. Lithos, 53(2), 81–100.

Sekine, T., Wyllie, P.J., 1982. Synthetic systems for modeling hybridization between hydrous siliceous magmas and peridotite in subduction zones. The Journal of Geology, 90, 734-741.

Sheldrick, G.M., 2003a. CELL_NOW, Program for unit cell determination. University of Göttingen, Germany.

Sheldrick, G.M. (2003b) SADABS, Program for empirical absorption correction of area detector data. University of Göttingen, Germany.

Sheldrick, G.M. (2008) A short history of SHELX. Acta Crystallographica Section A: Foundations of Crystallography 64(1), 112-122.

Signorelli, S., Vaggelli, G., and Romano, C. (1999) Pre-eruptive volatile (H_2O, F, Cl and S) contents of phonolitic magmas feeding the 3550-year old Avellino eruption from Vesuvius; southern Italy. Journal of Volcanology and Geothermal Research, 93, 237-256.

Sulpizio, R., Bonasia, R., Dellino, P., Mele, D., Di Vito, M.A., and La Volpe, L. (2010) The Avellino eruption of Somma–Vesuvius (3.9 ka BP). part II: sedimentology and physical volcanology of pyroclastic density current deposits. Bulletin of Volcanology, 72, 559-577, doi:10.1007/s00445-009-0340-4.

Uchida, E., Endo, S., and Makino, M. (2007) Relationship between solidification depth of granitic rocks and formation of hydrothermal ore deposits. Resource Geology 57, 47–56.

Vona, A., Romano, C., Giordano, G., and Sulpizio, R. (2020) Linking magma texture, rheology and eruptive style during the 472AD Pollena Subplinian eruption (Somma-Vesuvius). Lithos, 370-371, 105658.

Ventruti, G., Zema, M., Scordari, F., and Pedrazzi, G. (2008) Thermal behaviour of a Ti-rich phlogopite from Mt. Vulture (Potenza, Italy): An in situ X-ray single-crystal diffraction study. American Mineralogist 93, 632-643.

Young, E.D., and Morrison, J. (1992) Relations among net-transfer reaction progress, ^{18}O-^{13}C depletion, and fluid infiltration in a clinohumite-bearing marble. Contribution to Mineralogy and Petrology, 111, 391-408.

Warr, L.N. (2021) IMA–CNMNC approved mineral symbols. Mineralogical Magazine 85, 291-320, doi:10.1180/mgm.2021.43.

Waters, D.J., and Charnley, N.R. (2002) Local equilibrium in polymetamorphic gneiss and the titanium substitution in biotite. American Mineralogist, 87, 383-396.

Weiss, Z., Rieder, M., and Chmielová, M. (1992) Deformation of coordination polyhedra and their sheets in phyllosilicates. European Journal of Mineralogy, 4, 665-682.

Wu, C. M. (2015) Revised empirical garnet–biotite–muscovite–plagioclase geobarometer in metapelites. Journal of Metamorphic Geology, 33(2), 167-176.

Zollo, A., Gasparini, P., Virieux, J., Le Meur, H., Natale, G. de, Biella, G., Boschi, E., Capuano, P., Franco, R. de, dell'Aversana, P., Matteis, R. de, Guerra, I., Iannaccone, G., Mirabile, L., and Vilardo, G. (1996) Seismic evidence for a low-velocity zone in the upper crust beneath Mount Vesuvius. Science, 274, 592-594

LIST OF FIGURE CAPTIONS

Figure 1. Geological sketch map of Somma-Vesuvius (modified after Peccerillo, 2005) with samples provenance.

Figure 2. (a) Selected xenoliths from Somma-Vesuvius (see Table 1): PS44 (composite skarn-marble) and PS80 (cumulate) are from Pompeii eruption; PS57 (syenite) and PS77 (skarn) are from Avellino eruption (bar scale equal to 5 cm). (b) Distribution of the samples set according

to the lithotype and the occurrence.

Figure 3. Selected SEM micrographs (backscattered electrons, BSE mode) of mica-bearing xenoliths in thin sections. (a-h) skarn xenoliths; (i-m) skarn-marble xenoliths; (n) syenite skarns; (o,p) cumulate xenoliths. A thorough description of the mineral associations are given in the text. Mineral abbreviations (after Warr et al., 2021) are as in Table 1.

Figure 4. Selected major elements variations diagrams for the investigates Somma-Vesuvius xenoliths compared with literature data, (a) CaO against SiO_2 and (b) MgO against CaO (wt%).

Figure 5. Geochemical characteristics of the investigated mica-bearing xenoliths. (a) Chondrite-normalized REE and (b) primitive mantle-normalized minor to trace element patterns (normalization values from McDonough and Sun, 1995, and Lyubetskaya and Korenaga, 2007, respectively). Data from Vesuvius xenoliths (recent activity) of Balassone et al. (2013) are also reported.

Figure 6. SEM micrographs of micas from Somma-Vesuvius samples. (a) PS54; (b) PS57; (c) and (d) PS80, (Sdl, sodalite).

Figure 7. (a) Octahedral sheet composition of the studied micas in the *feal-mgli* plot, where *feal* = $^{[IV]}(Fe_{tot} + Mn + Ti - Al)$ and *mgli* = $^{[VI]}(Mg + Li)$ of Tischendorf et al. (2007). (b) Plot of tetrahedral Si vs. Al; the correlation between Si and total Al is reported in the inset. Symbols used for micas are the same as in Fig. 4.

Figure 8. Discrimination diagrams for the studied micas, Ti-^{VI}Al-F^--Mg#/2 (a) and Ba-Fe_{tot}-F^--Mg#

(b. The tetrahedral diagram has been made using the Tetra-Plot spreadsheet (Cucciniello, 2016). Symbols as in Fig. 4.

Figure 9. Plot of the $^{[XII]}Ba + {}^{[IV]}Al \leftrightarrow Si + {}^{[XII]}K$ substitution mechanism for the studied micas (symbols as in Fig. 4).

Figure 10. Plot of Al_2O_3 vs. TiO_2 (a) and FeO_t (b), as well as Mg # vs. TiO_2 (c) for micas of the present study, compared to selected Somma-Vesuvius micas composition from literature. Symbols explanation as in Fig. 4; black dotted line field = micas from AD 1872 eruption ejecta (Petti et al., 2010); grey solid line field = micas from skarn xenoliths mainly from Avellino, Pompeii and AD 472 Pollena eruptions (Gilg at al., 2001).

Figure 11. Plot of the *c* parameter vs. Mg number [$Mg/(Mg+Fe_{tot})$] for the investigated trioctahedral micas from the Avellino and Pompeii xenoliths (symbols as in Fig. 4). For comparison, values of phlogopite, fluorophlogopite and biotite of Vesuvius xenoliths from the AD 1631, AD 1872 and AD 1944 eruptions (Balassone et al., 2013) are reported.

LIST OF TABLE CAPTIONS

Table 1. Labels, occurrence, host rock and mineral assemblages of the Somma-Vesuvius samples. Sample provenances (see Fig. 1) are Somma Vesuviana and Ercolano (Avellino eruption) and Terzigno (Pompei eruption).

Table 2. Whole rock composition of the investigated mica-bearing xenoliths (major and minor elements in wt. % and trace elements in ppm).

Table 3. Chemical composition (EPMA, mean values on multiple point analyses expressed in wt% of oxides) of the investigated micas. Estimated values of formation temperature for selected samples are also given (see text for further explanation).

Table 4. Experimental details and relevant crystallographic data of the investigated micas.

Table 5. Selected bond distances (Å) and distortional parameters (calculated as reported in Lacalamita et al., 2011) of the studied mica crystals.

Table 6. Structural formulas in atoms per formula unit (apfu) of the selected micas for the crystallographic and crystal-chemical characterization.

Table 7. Mean atomic numbers (electrons, e^-) and average distances (Å) of cation sites derived by structure refinement (X-ref), and chemical data (EMPA) of the investigated mica crystals. Average error for mean atomic numbers is ± 0.5 e^-.

SUPPLEMENTAL MATERIALS

Supplemental Figure S1. Selected oxides of major and minor elements against SiO_2 and CaO (wt%) of Somma-Vesuvius xenoliths. Symbols as in Fig. 4.

Supplemental Figure S2. Selected trace elements plots against CaO (wt%) of Somma-Vesuvius xenoliths. Symbols as in Fig. 4.

Supplemental Figure S3. Plot of octahedral Al (a), Ti (b), and F (c) contents against Mg# for the studied micas (symbols as in Fig. 4).

Supplemental Figure S4. Plots of F vs. Ba for the studied micas (symbols as in Fig. 4).

Supplemental Figure S5. Plots of $Shift_{M2}$ (Å) parameter vs. Ti (a) and F^- (b) contents (apfu) and of α (°) parameter vs. Ti (c) and F^- (d) contents for the investigated trioctahedral micas from the Avellino and Pompeii xenoliths (see Tables 3 and 5). For comparison, values of phlogopite, fluorophlogopite, and biotite of Vesuvius xenoliths from the AD 1631, AD 1872 and AD 1944 eruptions (Balassone et al., 2013) are reported (symbols as in Fig. 4).

Supplemental Table S1. Chemical composition (wt% oxide) of miscellaneous silicates in the studied ejecta (mineral symbols as in Table 1; AV = Avellino eruption, PP = Pompeii eruption).

Supplemental Table S2. Chemical composition of phosphates and arsenates (wt% oxide) in the studied samples (mineral symbols as in Table 1; AV = Avellino eruption, PP = Pompeii eruption).

Supplemental Table S3. Chemical composition of oxides (wt% oxide) and sulfides (wt% elements) detected in the studied samples (mineral symbols as in Table 1; AV = Avellino eruption, PP = Pompeii eruption).

Supplemental Table S4. Chemical composition of carbonates (wt% oxide) in the studied samples (mineral symbols as in Table 1; AV = Avellino eruption, PP = Pompeii eruption).

CIF file: CIF FILES SV PHL.

This is the peer-reviewed, final accepted version for American Mineralogist, published by the Mineralogical Society of America.
The published version is subject to change. Cite as Authors (Year) Title. American Mineralogist, in press.
DOI: https://doi.org/10.2138/am-2022-8782. http://www.minsocam.org/

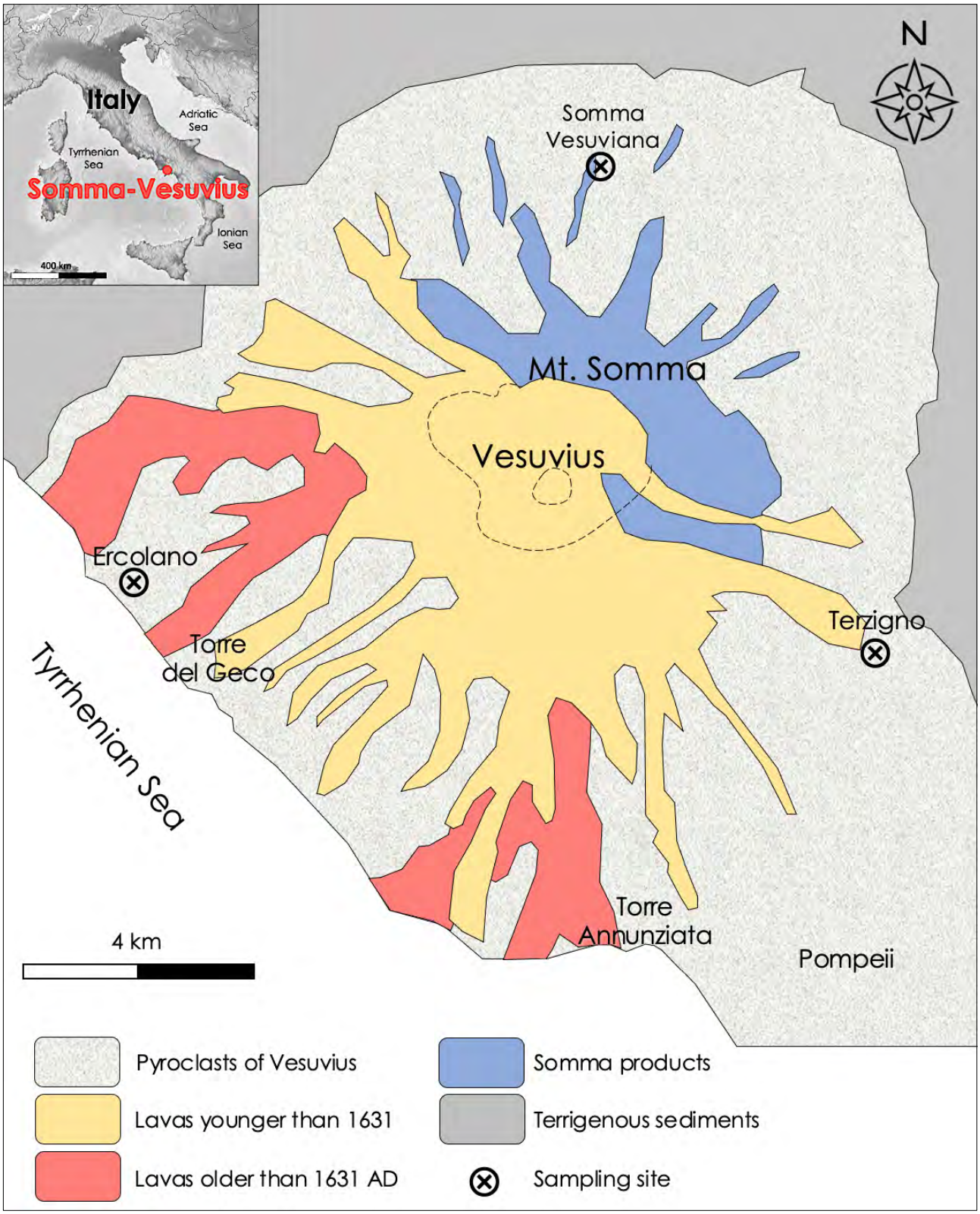

Figure 1

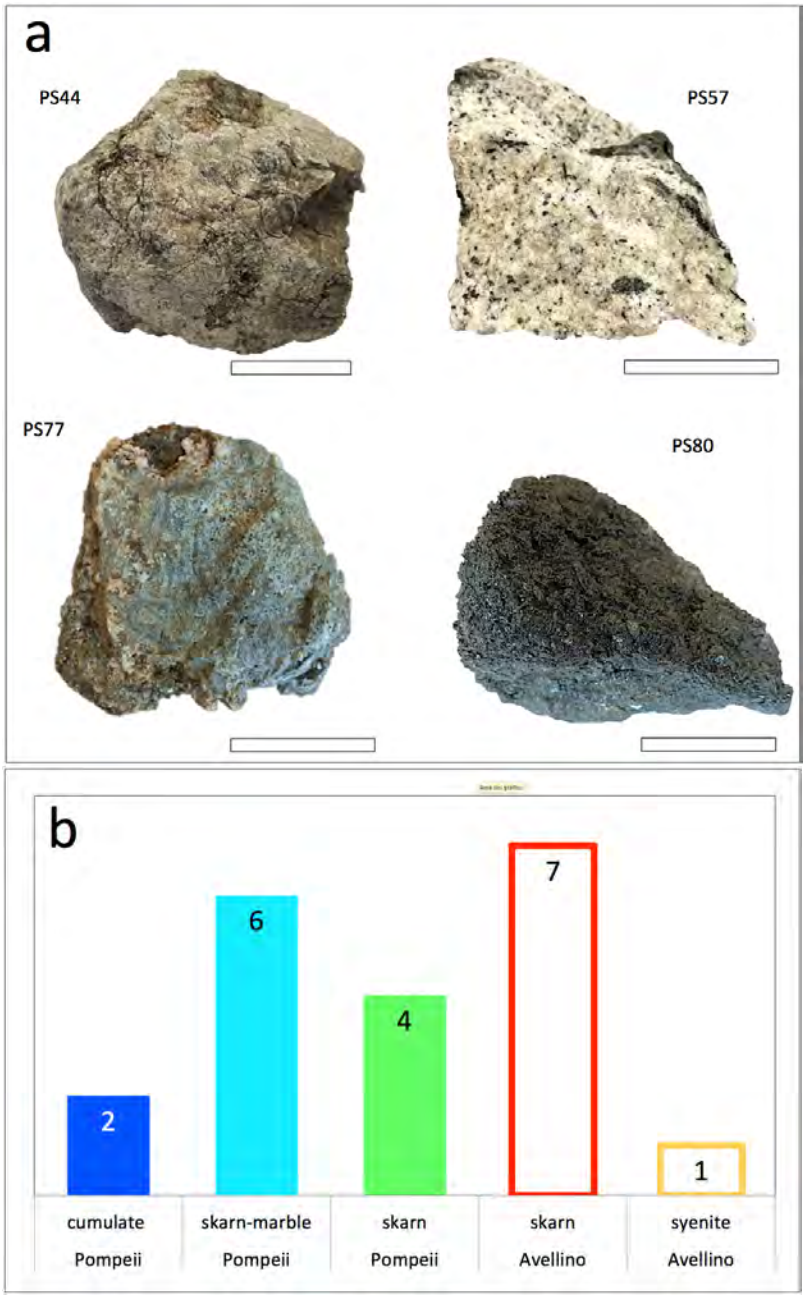

Figure 2

This is the peer-reviewed, final accepted version for American Mineralogist, published by the Mineralogical Society of America.
The published version is subject to change. Cite as Authors (Year) Title. American Mineralogist, in press.
DOI: https://doi.org/10.2138/am-2022-8782. http://www.minsocam.org/

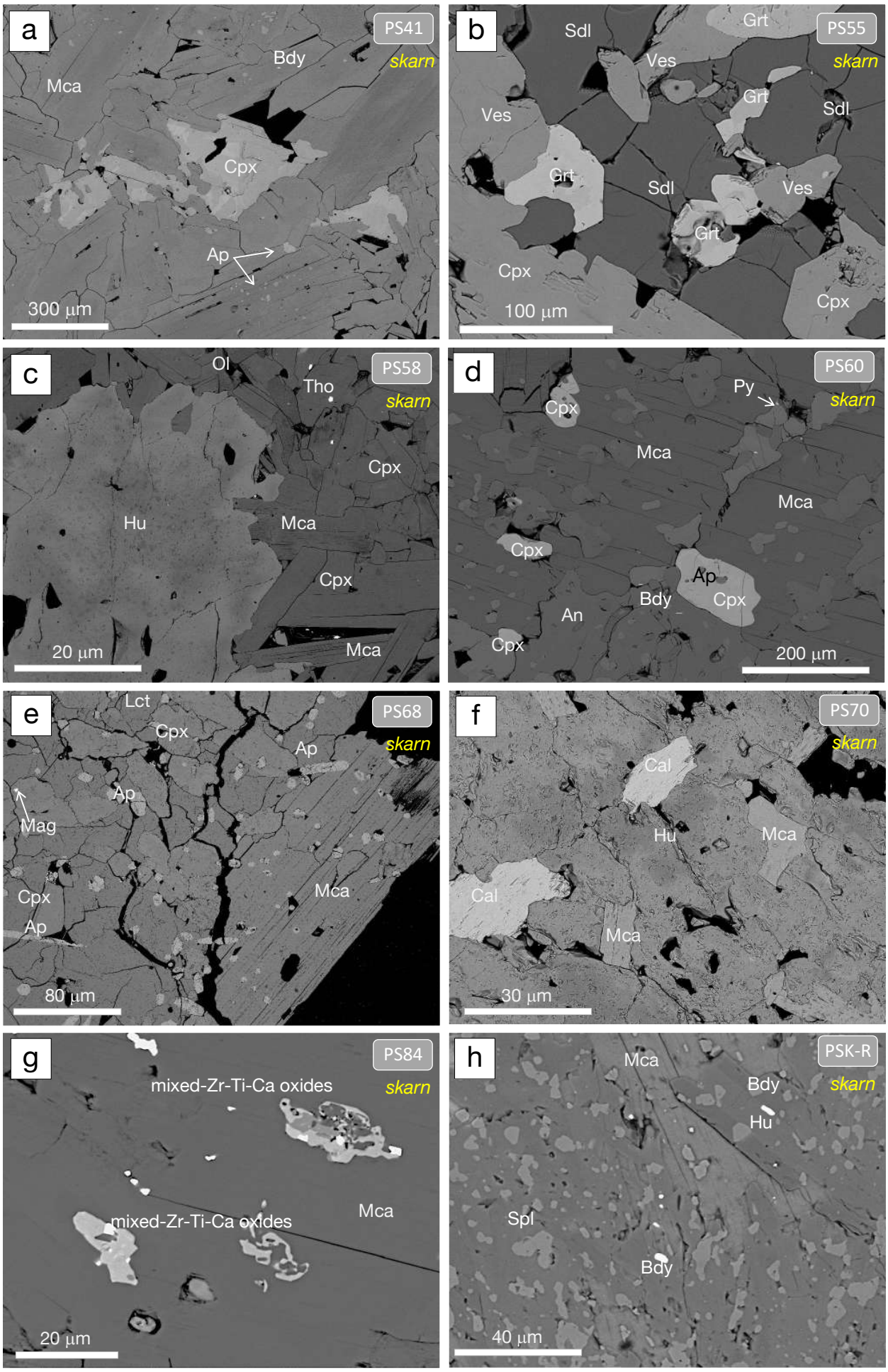

Fig. 3 (continued)

This is the peer-reviewed, final accepted version for American Mineralogist, published by the Mineralogical Society of America.
The published version is subject to change. Cite as Authors (Year) Title. American Mineralogist, in press.
DOI: https://doi.org/10.2138/am-2022-8782. http://www.minsocam.org/

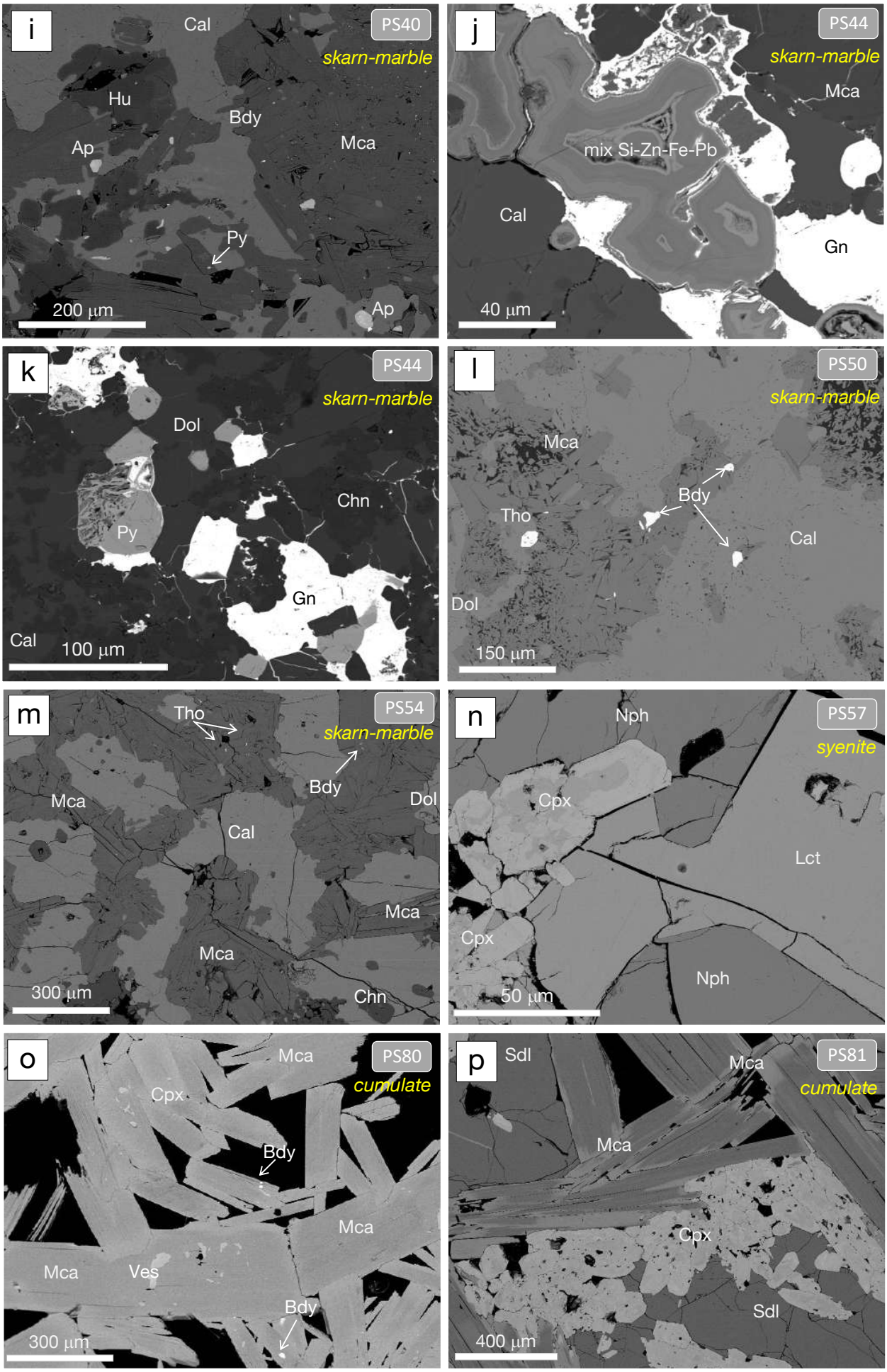

Fig. 3 (end)

This is the peer-reviewed, final accepted version for American Mineralogist, published by the Mineralogical Society of America.
The published version is subject to change. Cite as Authors (Year) Title. American Mineralogist, in press.
DOI: https://doi.org/10.2138/am-2022-8782. http://www.minsocam.org/

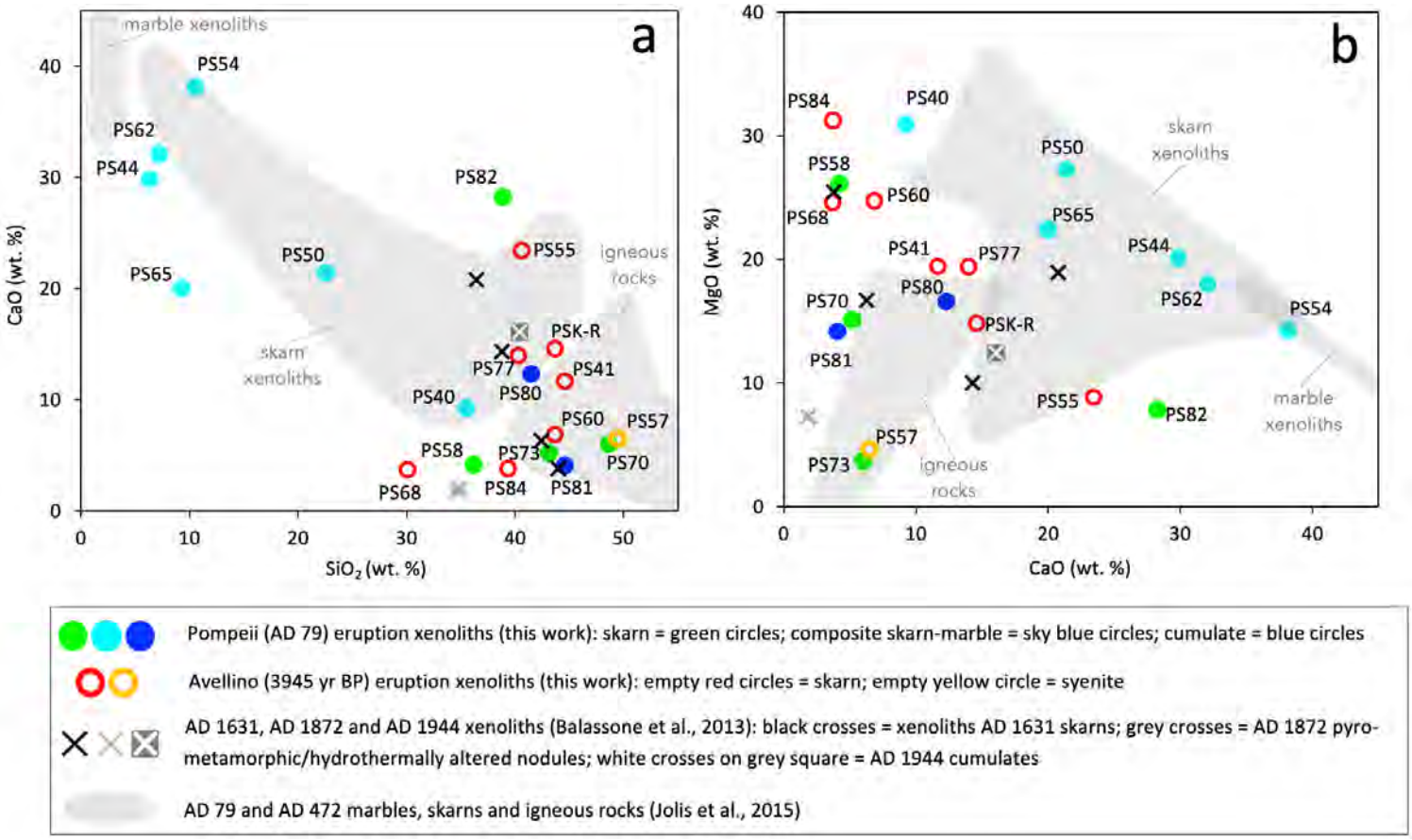

Figure 4

This is the peer-reviewed, final accepted version for American Mineralogist, published by the Mineralogical Society of America.
The published version is subject to change. Cite as Authors (Year) Title. American Mineralogist, in press.
DOI: https://doi.org/10.2138/am-2022-8782. http://www.minsocam.org/

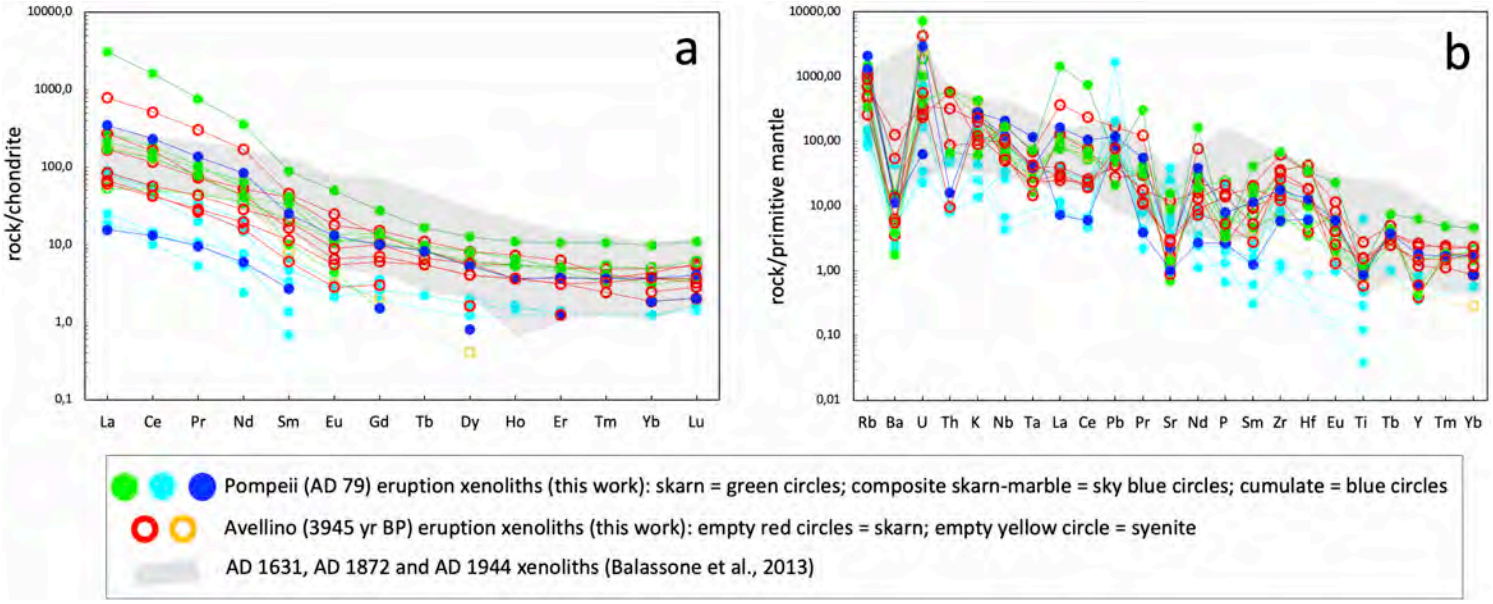

Figure 5

This is the peer-reviewed, final accepted version for American Mineralogist, published by the Mineralogical Society of America.
The published version is subject to change. Cite as Authors (Year) Title. American Mineralogist, in press.
DOI: https://doi.org/10.2138/am-2022-8782. http://www.minsocam.org/

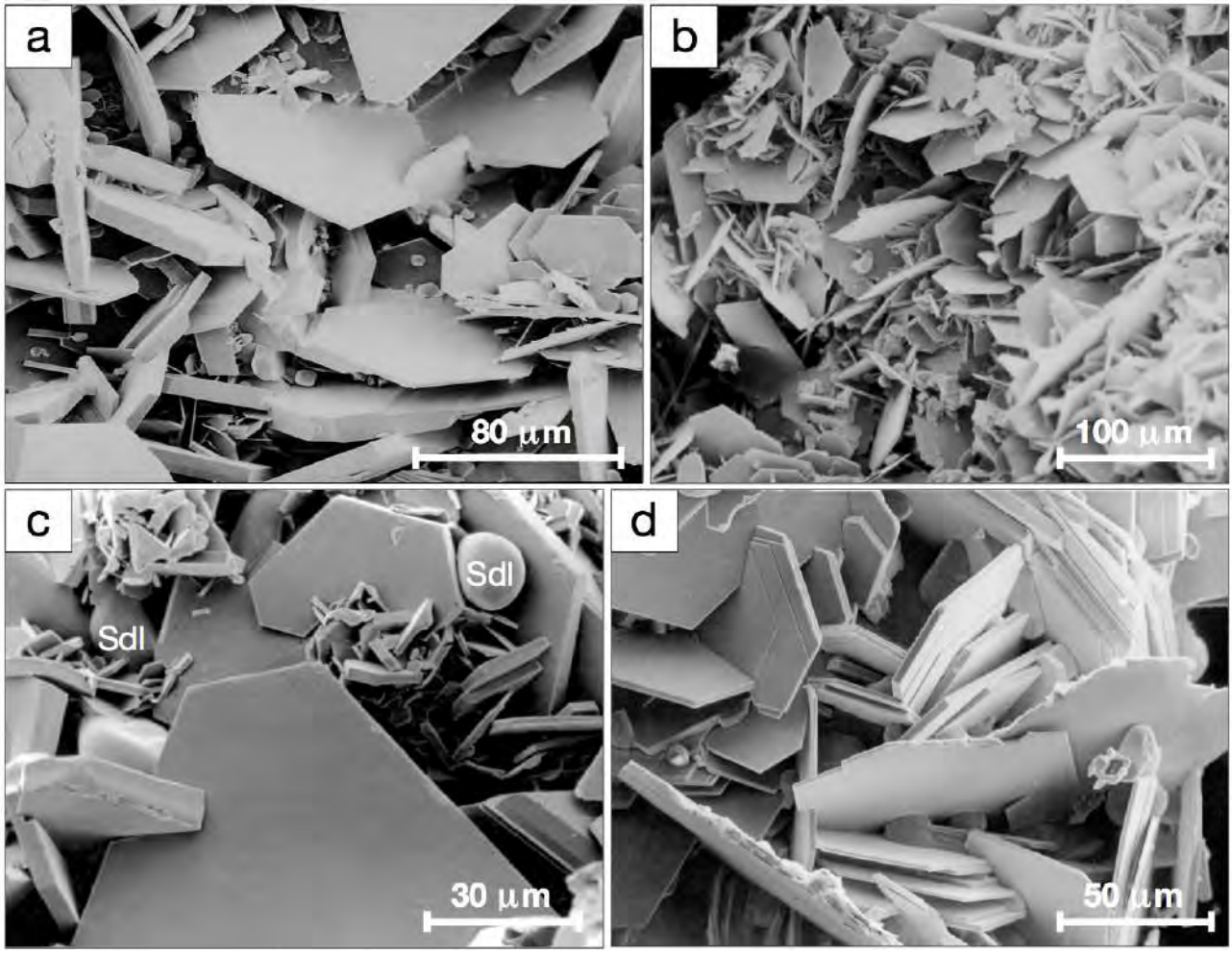

Figure 6

This is the peer-reviewed, final accepted version for American Mineralogist, published by the Mineralogical Society of America.
The published version is subject to change. Cite as Authors (Year) Title. American Mineralogist, in press.
DOI: https://doi.org/10.2138/am-2022-8782. http://www.minsocam.org/

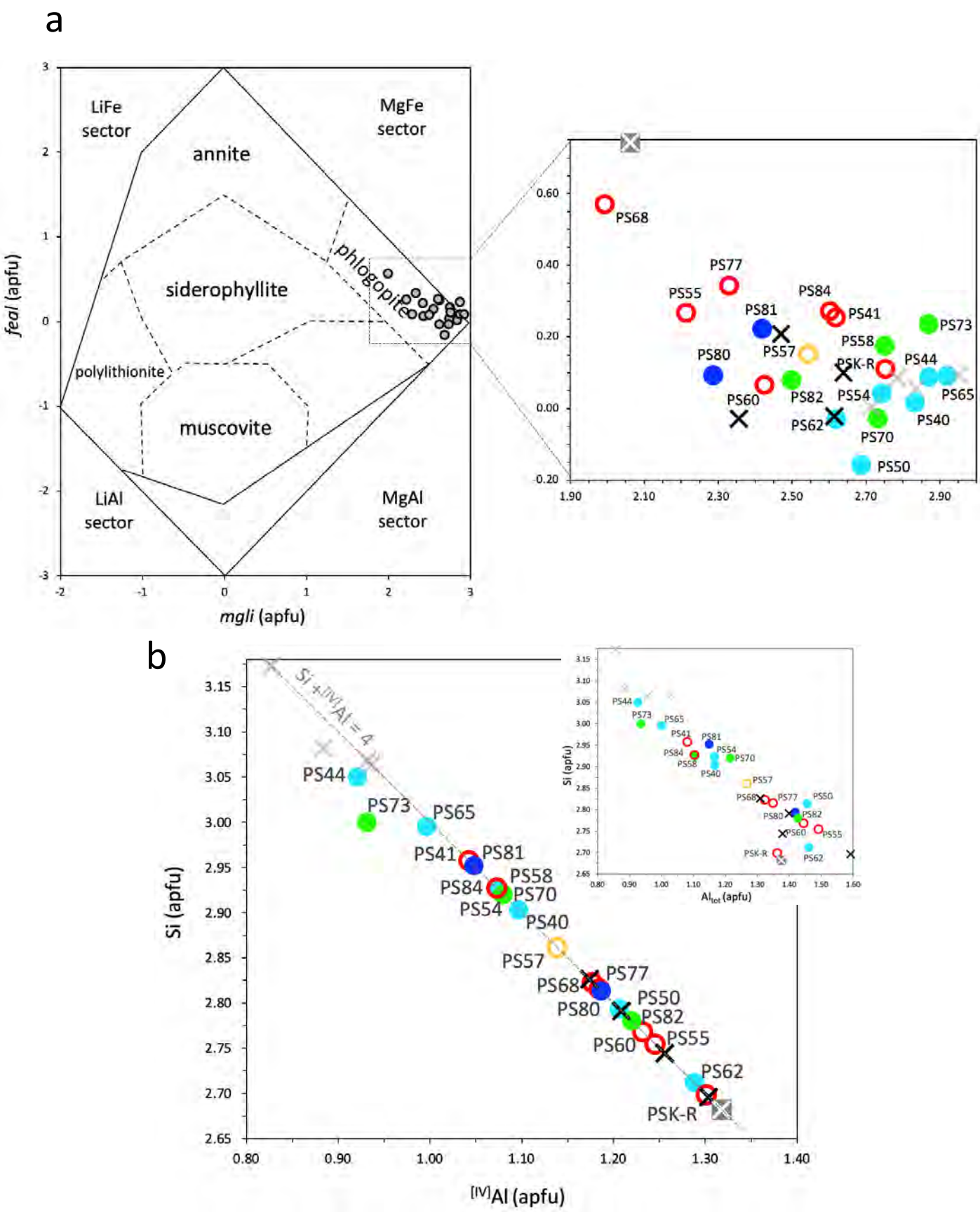

Figure 7

This is the peer-reviewed, final accepted version for American Mineralogist, published by the Mineralogical Society of America.
The published version is subject to change. Cite as Authors (Year) Title. American Mineralogist, in press.
DOI: https://doi.org/10.2138/am-2022-8782. http://www.minsocam.org/

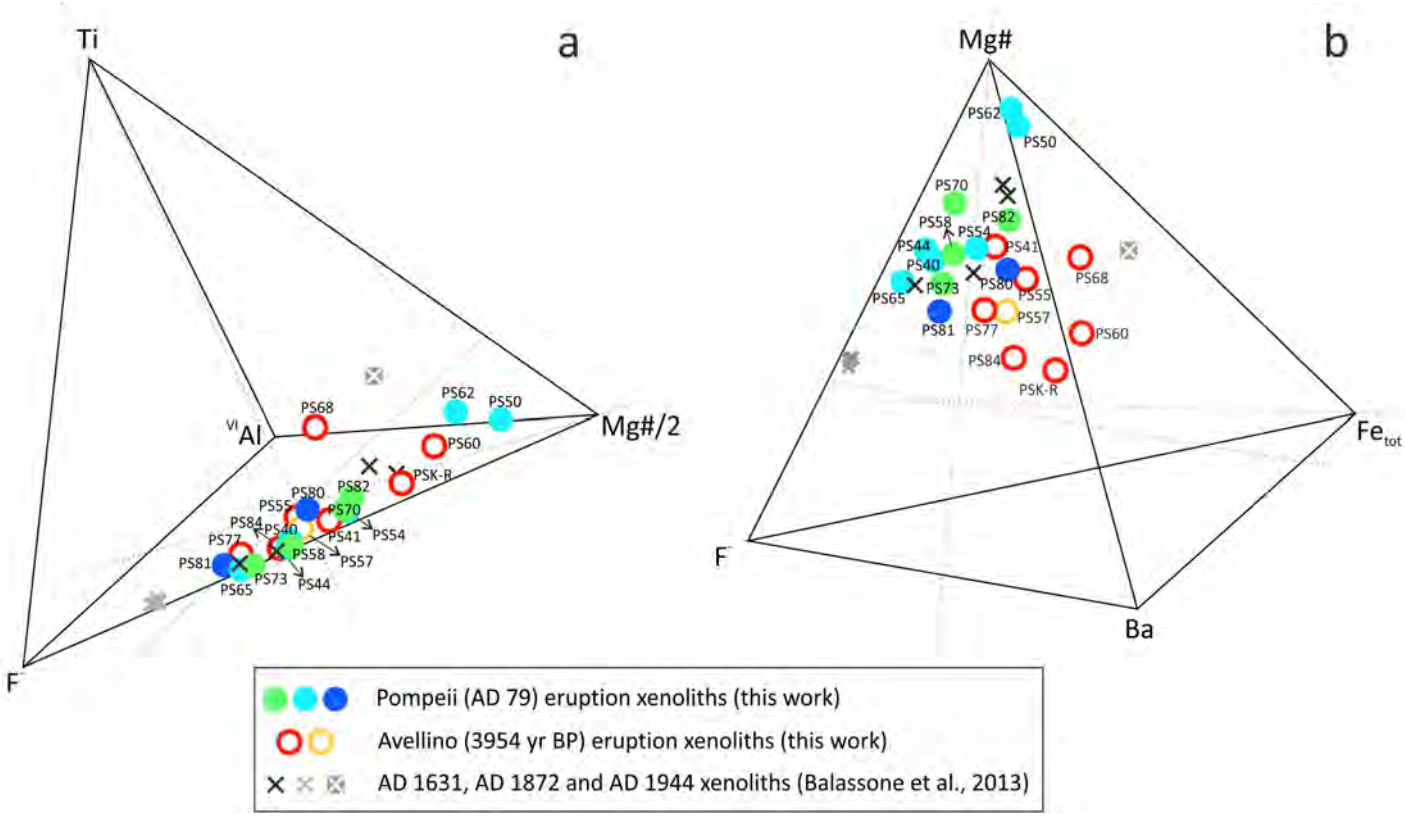

Figure 8

This is the peer-reviewed, final accepted version for American Mineralogist, published by the Mineralogical Society of America.
The published version is subject to change. Cite as Authors (Year) Title. American Mineralogist, in press.
DOI: https://doi.org/10.2138/am-2022-8782. http://www.minsocam.org/

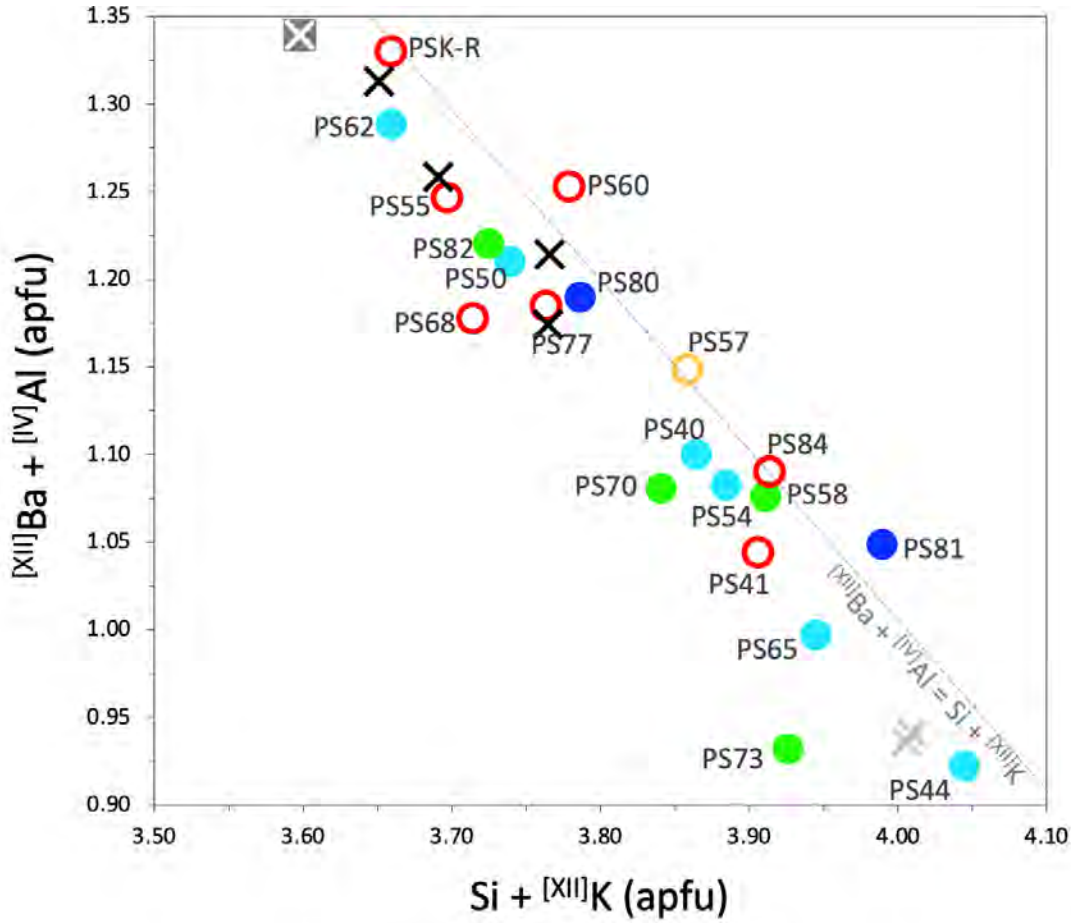

Figure 9

This is the peer-reviewed, final accepted version for American Mineralogist, published by the Mineralogical Society of America.
The published version is subject to change. Cite as Authors (Year) Title. American Mineralogist, in press.
DOI: https://doi.org/10.2138/am-2022-8782. http://www.minsocam.org/

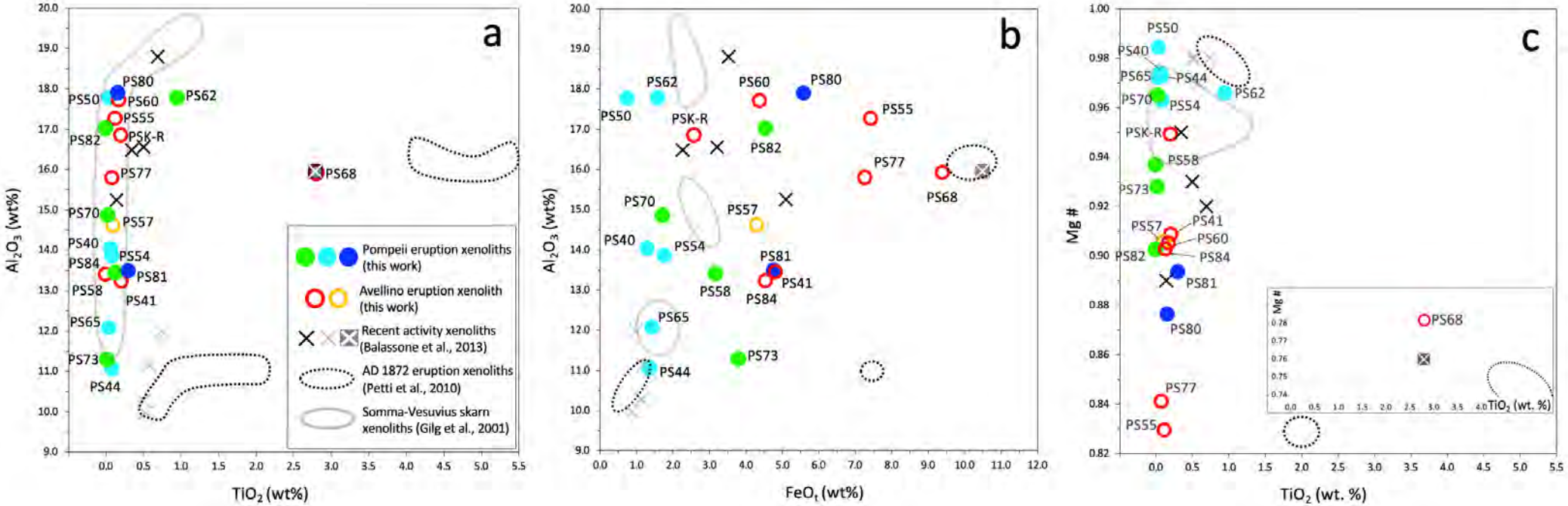

Figure 10

This is the peer-reviewed, final accepted version for American Mineralogist, published by the Mineralogical Society of America.
The published version is subject to change. Cite as Authors (Year) Title. American Mineralogist, in press.
DOI: https://doi.org/10.2138/am-2022-8782. http://www.minsocam.org/

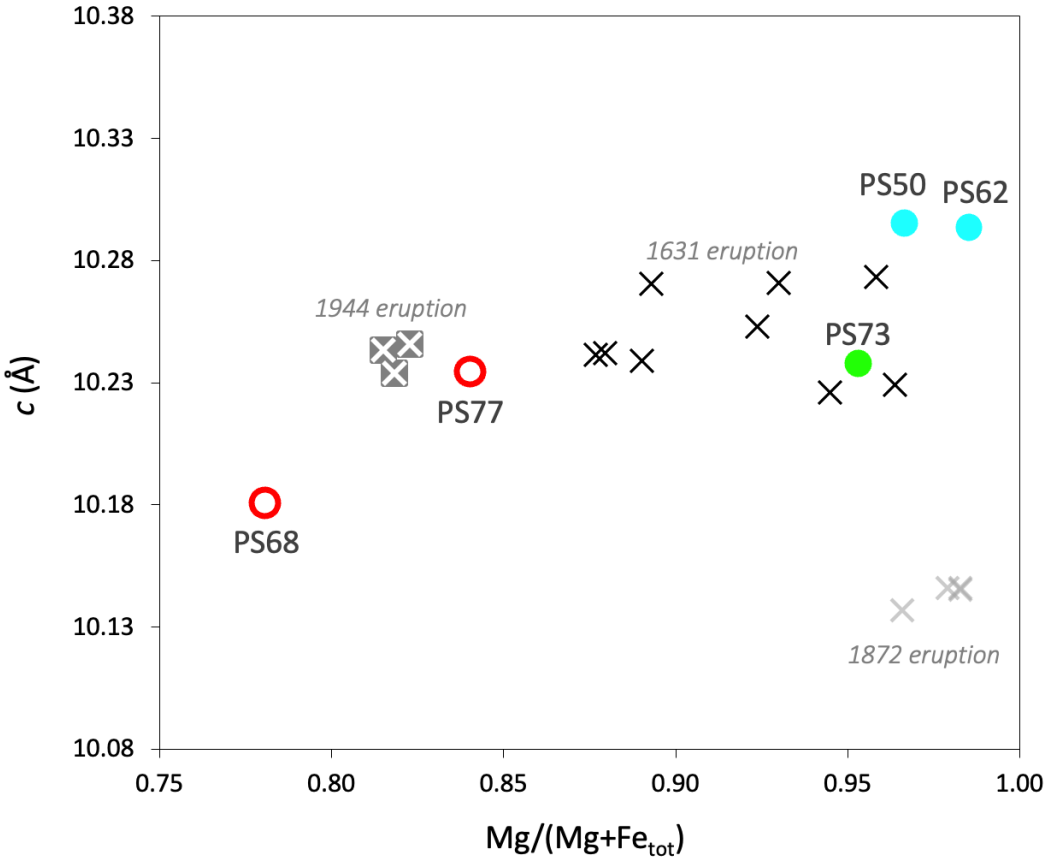

Figure 11

Table 4
Experimental details and relevant crystallographic data of the studied crystals.

	Avellino xenoliths		Pompeii xenoliths		
	PS68	PS77	PS50	PS62	PS73
Crystallographic data					
Space group	*C2/m*	*C2*	*C2/m*	*C2/m*	*C2/m*
a (Å)	5.3169(1)	5.3218(1)	5.3072(2)	5.3055(1)	5.3188(1)
b (Å)	9.2041(2)	9.2188(4)	9.1945(3)	9.1893(1)	9.2104(1)
c (Å)	10.1803(2)	10.2343(2)	10.2932(4)	10.2951(2)	10.2376(1)
β (°)	99.983(2)	100.011(2)	99.942(2)	99.902(1)	99.978(1)
Cell volume ($Å^3$)	490.65(2)	494.46(2)	494.74(3)	494.45(2)	493.94(1)
Z	4	4	4	4	4
Experimental details					
Reflections collected	5033	6066	3816	6048	6117
Reflections unique	1256	1829	1292	1805	1787
$R_{merging}$ [$R_{(int)}$] (%)	2.79	2.76	2.26	1.79	1.86
Reflections used (I>3σ(I))	953	1333	1124	1585	1432
No. of refined parameters	56	71	58	56	56
Goof[a]	1.087	0.983	0.965	0.947	1.045
R_1[b] (%)	2.66	2.85	3.27	1.98	2.63
wR_2[c] (%)	3.23	4.23	4.96	2.39	3.50
$\Delta\rho_{min}/\Delta\rho_{max}$ ($e^-/Å^3$)	-0.41/0.71	-0.51/1.01	-0.53/0.96	-0.44/0.49	-0.39/1.38

a: Goodness-of-fit = $[\Sigma[w(F_o^2-F_c^2)^2]/(N\text{-p})]^{1/2}$, where N and p are the number of reflections and parameters. respectively.
b: $R_1 = \Sigma[|F_o| - |F_c|]/\Sigma|F_o|$.
c: $wR_2 = [\Sigma[w(F_o-F_c)^2]/\Sigma[w(F_o)^2]]^{1/2}$; w = Chebyshev optimized weights.

Table 5
Selected bond distances (Å) and distortional parameters (calculated as reported in Lacalamita et al. 2011) of the studied crystals.

	Avellino xenoliths		Pompeii xenoliths		
	PS68	PS77	PS50	PS62	PS73
T-O1	1.656(2)	1.660(2)	1.664(2)	1.6660(5)	1.6572(8)
T-O1'	1.656(2)	1.661(2)	1.666(2)	1.6669(5)	1.6577(8)
T-O2	1.656(1)	1.6594(9)	1.666(1)	1.6668(3)	1.6584(5)
T-O3	1.670(2)	1.661(1)	1.660(2)	1.6681(5)	1.6504(7)
<T-O>	1.660(4)	1.660(3)	1.664(4)	1.6670(9)	1.656(1)
M1-O4(x2)	2.031(2)	2.048(2)	2.043(3)	2.0420(6)	2.0454(8)
M1-O3(x4)	2.086(1)	2.083(1)	2.079(2)	2.0737(5)	2.0853(6)
<M1-O>	2.068(2)	2.071(2)	2.067(4)	2.0631(8)	2.072(1)
M2-O4(x2)	1.987(2)	2.057(1)	2.057(2)	2.0495(5)	2.0558(6)
M2-O3(x2)	2.081(1)	2.071(1)	2.063(2)	2.0587(5)	2.0741(7)
M2-O3'(x2)	2.112(2)	2.071(1)	2.077(2)	2.0721(5)	2.0848(6)
<M2-O>	2.060(3)	2.066(2)	2.065(3)	2.0601(9)	2.072(1)
<M-O>	2.063(4)	2.068(3)	2.066(5)	2.061(1)	2.072(1)
K-O1(x4)	2.946(2)	2.962(2)	2.929(2)	2.9121(5)	2.9834(9)
K-O1'(x4)	3.346(2)	3.368(2)	3.428(2)	3.4566(6)	3.3380(9)
K-O2 (x2)	2.948(3)	2.961(2)	2.926(3)	2.9111(7)	2.981(1)
K-O2'(x2)	3.362(3)	3.368(2)	3.429(3)	3.4594(9)	3.338(1)
$<K\text{-}O>_{inner}$	2.947	2.962(3)	2.928	2.912	2.9826
$<K\text{-}O>_{outer}$	3.351	3.368(3)	3.428	3.458	3.338
<K-O>	3.149		3.178	3.185	3.160
T_D-O1		1.65(4)			
T_D-O11		1.61(4)			
T_D-O2		1.72(5)			
T_D-O3		1.66(1)			
$<T_D\text{-}O>$		1.67(7)			
K_D-O1 (x2)		2.31(1)			
K_D-O1'(x2)		2.307(6)			
K_D-O2(x2)		2.32(2)			
K_D-O2'(x2)		3.02(5)			
K_D-O11 (x2)		2.96(4)			
K_D-O11'(x2)		3.36(4)			
$<K_D\text{-}O>_{inner}$					
$<K_D\text{-}O>_{outer}$					
α (°)	8.86	8.94	11.06	11.53	8.80
$Volume_T$ (Å^3)	2.344	2.347	2.363	2.367	2.340
BLD_T	0.302	0.032	0.105	0.190	0.349
$Volume_{M1}$ (Å)	11.556	11.638	11.581	11.491	11.665
$BLD_{M(1)}$	1.172	0.733	0.774	0.670	0.857
$Volume_{M2}$ (Å)	11.433	11.608	11.552	11.446	11.659
$BLD_{M(2)}$	2.392	0.409	0.343	0.393	0.519
$Shift_{M2}$ (Å)	0.062	-0.019	-0.019	-0.017	-0.016
$\Delta_{K\text{-}O}$ (Å)	0.404	0.406	0.500	0.520	0.400

Errors on distortion parameters, estimated by varying the refined positional parameters within one standard deviation are in the following ranges: < 0.5% for volumes and shifts; 0.1-13% for α and $\Delta_{K\text{-}O}$.

Table 6
Structural formulas in atoms per formula unit (apfu) of the selected micas for the crystallographic and crystal-chemical characterization.

	Sample	
Avellino xenoliths	PS68	$(K_{0.89}Na_{0.04})_{\Sigma=0.93}(Mg_{2.03}Fe^{2+}_{0.09}Fe^{3+}_{0.48}Mn_{0.01}Al_{0.23}Ti_{0.15})_{\Sigma=2.99}(Si_{2.88}Al_{1.12})_{\Sigma=4.00}O_{10.83}F_{0.25}Cl_{0.01}OH_{0.91}$
	PS77	$(K_{0.94}Na_{0.06})_{\Sigma=1.00}(Mg_{2.32}Fe^{2+}_{0.37}Fe^{3+}_{0.07}Mn_{0.06}Al_{0.16})_{\Sigma=2.98}(Si_{2.80}Al_{1.20})_{\Sigma=4.00}O_{10.03}F_{0.71}OH_{1.26}$
Pompeii xenoliths	PS50	$(K_{0.95}Na_{0.08}Ca_{0.02})_{\Sigma=1.05}(Mg_{2.70}Fe^{3+}_{0.04}Al_{0.24}Mn_{0.01})_{\Sigma=2.99}(Si_{2.81}Al_{1.19})_{\Sigma=4.00}O_{10.16}OH_{1.84}$
	PS62	$(K_{0.95}Na_{0.02})_{\Sigma=0.97}(Mg_{2.62}Fe^{3+}_{0.09}Al_{0.18}Cr_{0.05}Ti_{0.05})_{\Sigma=2.99}(Si_{2.71}Al_{1.29})_{\Sigma=4.00}O_{10.10}F_{0.04}OH_{1.86}$
	PS73	$(K_{0.92}Na_{0.06})_{\Sigma=0.98}(Mg_{2.85}Fe^{3+}_{0.14}Mn_{0.01})_{\Sigma=3.00}(Si_{2.98}Al_{0.93}Fe^{3+}_{0.09})_{\Sigma=4.00}O_{10.10}F_{0.69}OH_{1.21}$

Table 7

Mean atomic numbers (electrons, e^-) and average distances (Å) of cation sites derived by structure refinement (X-ref), and chemical data (EMPA). Average error for mean atomic numbers is $\pm$ 0.5 e^-.

	Avellino xenoliths		Pompeii xenoliths		
	PS68	PS77	PS50	PS62	PS73
T $e^-_{X\text{-}ref}$	14.00	14.24	14.00	14.00	14.00
T e^-_{EPM}	13.72	13.70	13.70	13.68	14.04
$e^-_{(M1+2M2)\ X\text{-}ref}$	45.34	41.47	36.94	39.01	38.07
$e^-_{(M1+2M2)\ EMPA}$	45.72	42.86	36.91	38.42	38.09
K $e^-_{X\text{-}ref}$	17.92	17.61	16.89	18.89	17.23
K e^-_{EMPA}	17.35	18.52	19.33	18.27	18.14
$\langle T\text{-}O\rangle_{X\text{-}ref}$	1.660	1.660	1.664	1.667	1.656
$\langle T\text{-}O\rangle_{EMPA}$	1.656	1.659	1.659	1.662	1.655
$\langle M\text{-}O\rangle_{X\text{-}ref}$	2.063	2.068	2.066	2.061	2.072
$\langle M\text{-}O\rangle_{EMPA}$	2.054	2.075	2.068	2.067	2.079